VYSOKÉ UČENÍ TECHNICKÉ V BRNĚ

BRNO UNIVERSITY OF TECHNOLOGY

FAKULTA STROJNÍHO INŽENÝRSTVÍ
ÚSTAV FYZIKÁLNÍHO INŽENÝRSTVÍ

FACULTY OF MECHANICAL ENGINEERING
INSTITUTE OF PHYSICAL ENGINEERING

APLIKACE GRAFÉNOVÉ MEMBRÁNY V NANOELEKTRONICKÝCH ZAŘÍZENÍCH

APPLICATION OF GRAPHENE MEMBRANE IN NANOELECTRONIC DEVICES

DIPLOMOVÁ PRÁCE
MASTER'S THESIS

AUTOR PRÁCE — Bc. LUKÁŠ KORMOŠ
AUTHOR

VEDOUCÍ PRÁCE — Ing. MIROSLAV BARTOŠÍK, Ph.D.
SUPERVISOR

BRNO 2015

Vysoké učení technické v Brně, Fakulta strojního inženýrství

Ústav fyzikálního inženýrství
Akademický rok: 2014/2015

ZADÁNÍ DIPLOMOVÉ PRÁCE

student(ka): Bc. Lukáš Kormoš

který/která studuje v **magisterském navazujícím studijním programu**

obor: **Fyzikální inženýrství a nanotechnologie (3901T043)**

Ředitel ústavu Vám v souladu se zákonem č.111/1998 o vysokých školách a se Studijním a zkušebním řádem VUT v Brně určuje následující téma diplomové práce:

Aplikace grafénové membrány v nanoelektronických zařízeních

v anglickém jazyce:

Application of Graphene Membrane in Nanoelectronic Devices

Stručná charakteristika problematiky úkolu:

Transportní vlastnosti grafénu [1] jsou silně ovlivněny přítomností podložního substrátu, který značně limituje pohyblivost nosičů náboje [2,3], způsobuje jeho dopování dírami případně elektrony (posun Fermiho meze vůči Diracovu bodu) a mění samotnou pásovou strukturu grafénu, což v konečném důsledku ničí přednosti grafénu při jeho použití v reálných nanoelektronických zařízeních. Řešení tohoto problému představuje použití zavěšeného grafénu neboli grafénové membrány, čímž se zabývá tato diplomová práce.

Cíle diplomové práce:

1. Proveďte literární rešerši uvedené problematiky.
2. Optimalizujte výrobu CVD grafénové membrány.
3. Ověřte kvalitu membrány pomocí transportních měření.
4. Porovnejte výsledky s grafénem na podložním substrátu SiO2.
5. Diskutujte použití membrány v zařízeních na bázi grafénu zkoumaných na ÚFI (senzory, polem řízené tranzistory).

Seznam odborné literatury:

[1] NOVOSELOV, K. S., et al.: Two-dimensional gas of massless Dirac fermions in graphene, Nature, Vol. 438, 2005, p. 197-200
[2] K.I. BOLOTIN, K.J., et al.: Ultrahigh electron mobility in suspended graphene, Solid State Communications, Vol. 146, 2008, p. 351-355
[3] DU X.,SKACHKO I. I.,BARKER A., ANDREI E.Y. : Approaching Ballistic Transport in Suspended Graphene, Nature Nanotechnology, Vol. 3, 2008, p. 491 - 495

Vedoucí diplomové práce: Ing. Miroslav Bartošík, Ph.D.

Termín odevzdání diplomové práce je stanoven časovým plánem akademického roku 2014/2015.

V Brně, dne 24.11.2014

L.S.

prof. RNDr. Tomáš Šikola, CSc. Ředitel ústavu	doc. Ing. Jaroslav Katolický, Ph.D. Děkan fakulty

ABSTRACT

This master's thesis is focused on applications and fabrication of a graphene membrane from graphene prepared by chemical vapor deposition. Theoretical part deals with transport properties of graphene and multiple scattering processes limiting charge carrier mobility in this material. Moreover, a short review of graphene membrane applications is included. Experimental part provides a description of a process, which is used for fabrication of a suspended graphene device. Electron beam lithography, focused ion beam milling, chemical etching and patterning of graphene by oxygen plasma are utilized. The graphene membranes are characterised by transport properties measurement and compared with non-suspended graphene.

KEYWORDS

graphene, graphene membrane, chemical vapor deposition, CVD, electron beam lithography, EBL, transport properties

ABSTRAKT

Táto diplomová práca je zameraná na aplikácie a výrobu grafénovej membrány z grafénu vyrobeného pomocov chemickej depozície z plynnej fáze. Teoretická časť sa zaoberá transportnými vlastnosťami grafénu a mnohonásobnými rozptylovými procesmi, ktoré obmedzujú pohyblivosť nosičov náboja v tomto materiáli. Ďalej je zahrnutá krátka recenzia aplikácií grafénových membrán. Experimentálna časť prezentuje výrobný proces pre dosiahnutie zaveseného grafenového zariadenia s využitím elektrónové litografie, fokusovaného zväzku iónov, chemického leptania a tvarovania grafenovej vrstvy. Grafénová membrána je charakterizovaná meraním transportných vlastností a tieto sú následne porovnané s grafénom položeným na substráte.

KLÍČOVÁ SLOVA

grafén, grafénová membrána, chemická depozícia z plynnej fáze, CVD, elektrónová litografia, EBL, transportné vlastnosti

KORMOŠ, Lukáš *Application of Graphene Membrane in Nanoelectronic Devices*: master's thesis. Brno: Brno University of Technology, Faculty of Electrical Engineering and Communication, Institute of Physical Engineering, 2015. 59 p. Supervised by Ing. Miroslav Bartošík, Ph.D.

DECLARATION

I declare that I have written my master's thesis on the theme of "Application of Graphene Membrane in Nanoelectronic Devices" independently, under the guidance of the master's thesis supervisor and using the technical literature and other sources of information which are all quoted in the thesis and detailed in the list of literature at the end of the thesis.

Brno ....

(author's signature)

ACKNOWLEDGEMENT

I would like to thank Ing. Miroslav Bartošík, Ph.D. for his guidance and patience during the creation of this master's and the endless proofreading. Further, I want to thank Ing. Pavel Procházka for fabrication of the graphene and his help and advice with the transport measurements. Special thanks go to all the great people at the Institute of Physical Engineering and particularly to Ing. Zuzana Lišková, Ing. Mgr. Tomáš Šamořil and Ing. Martin Konečný for helpful discussions and advice.
Separate category are my classmates to whom I want to thank for great five years of "studying". To have a class full of friends is a phenomenal fun. Specifically, I want to thank Andrea Konečná and Michal Kern$^{san\ dan}$ for their bravery in proofreading of the text and Lukáš Flajšman and Marek Vaňatka for their everlasting presence in the lab (or around) which made the work much easier.
Veľké vďaka tiež patrí mojej rodine za ich podporu a pochopenie počas celého štúdia.

Lukáš Kormoš

Part of this work was carried out with the support of Structural Analysis Laboratory of CEITEC – Central European Institute of Technology under CEITEC – open access project, ID number LM2011020, funded by the Ministry of Education, Youth and Sports of the Czech Republic.
This work was also supported by project Advanced Microscopy and Spectroscopy Platform for Research and Development in Nano and Microtechnologies, funded by Technology Agency of the Czech Republic (grant No. TE01020233).

CONTENTS

INTRODUCTION

Graphene is a two dimensional arrangement of carbon atoms in a honeycomb crystal lattice. It was first discovered in 2004 by a research group in Manchester led by A. Geim and K. Novoselov [1]. They have reported fabrication of atomically thin layer of carbon atoms on a silicon oxide substrate by micromechanical cleavage of graphite. Graphene quickly raised attention in scientific community for its outstanding optical, electrical [2] and mechanical properties [3]. Importance of this discovery was highlighted by awarding of the Nobel Prize in Physics to A. Geim and K. Novoselov for "for groundbreaking experiments regarding the two-dimensional material graphene" [4].

Graphene proved to be a suitable candidate for broad range of applications. Specifically in electronics it is supposed to be a replacement for current silicon based technologies, e.g. graphene field effect transistor was reported with 100 Ghz operational frequency [5]. Another advantage is the ultimate thickness of graphene, which allows for downscaling the device size. Carbon based material are also common and mostly inexpensive resource which could lead to long term and sustainable utilization of graphene.

One of the main methods for characterisation of graphene quality is the charge carrier mobility. The mobility of graphene on SiO_2 substrate is assumed to be limited by extrinsic scattering by surface phonons to a value of $40\,000\,\mathrm{cm^2V^{-1}s^{-1}}$ [6]. Therefore, the substrate choice is important to fabricate high speed electronics, with low charge scattering. Another possibility, how to remove the limitations caused by the substrate, is to prepare a suspended graphene device shown in Fig.1. Similar devices prepared from exfoliated graphene were reported with mobility of $200\,000\ \mathrm{cm^2V^{-1}s^{-1}}$ [7]. Only with a high carrier mobility guarantees the observation of extraordinary graphene properties, e.g., the symmetry-broken quantum Hall effect, the integer quantum Hall effect (IQHE) or the Klein tunnelling.

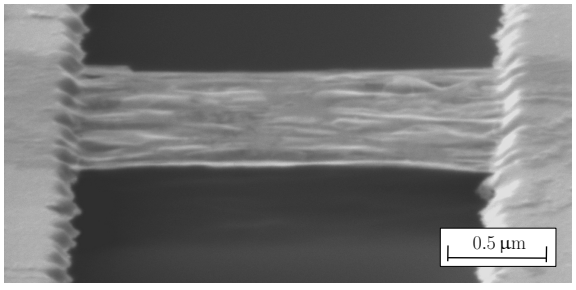

Fig. 1: SEM image of graphene membrane prepared by etching of the substrate. Graphene is supported by golden electrodes on the sides and the length of the membrane is 2.8 µm.

The most promising graphene fabrication method for commercial applications is a chemical vapor deposition (CVD). This method allows to prepare large scale graphene layers with dimensions in tens of centimetres [8]. Compared to exfoliated graphene, the CVD process results in polycrystalline graphene layer. Additionally, crystal defects and chemical residues from fabrication process can aggravate electronic properties of graphene.

The aim of this thesis is to develop a process that enables the fabrication of suspended CVD graphene devices. Removing the substrate should allow better utilization of the intrinsic electronic properties of CVD graphene.

Description of graphene structure and its fundamental electronic properties are detailed in the first chapter of this thesis. Since this work is focused on electronic properties of graphene, second chapter is dedicated to description of charge carrier mobility and scattering effects present in graphene layer. Third chapter describes the applications of graphene membranes. This chapter includes description of some mechanical properties of graphene, e.g., tensile strength and thermal expansion. Additionally, it shows the diversity present in the current research of graphene.

Experimental part describes fabrication process of a graphene membrane supported by gold electrodes. In the last chapter, fabricated graphene membranes are characterised by measurement of their transport properties.

1 GRAPHENE

1.1 Carbon

Carbon is often referred to as the basic element of life and belongs to the most common elements on Earth. Large part of chemistry, organic chemistry, is dedicated to study of carbon and hydrogen compounds and their derivatives. The number of known carbon-based chemical compounds grows into millions. The special nature of carbon chemical reactivity is given by its ability to reconfigure its valence shell and to form long chained molecules [9].

1.1.1 Electronic structure

Electron configuration of carbon in its ground state is $1s^2\,2s^2\,2p^2$. Carbon in this state has two valence electrons in the $2p$ orbital available for bonding. This divalent form of carbon occurs in some transient-organic intermediates, e.g. carbenes, which are highly reactive. However, carbon has usually tetravalent nature (forms four chemical bonds), because of its hybridized electron orbitals. Several hybridizations exist, labelled by electrons which are combined to form them: sp, sp^2 and sp^3. In diamond structures or simple methane, carbon possess tetrahedral symmetry and creates four covalent σ bonds, therefore has sp^3 hybridization. The basis of all graphitic structures and aromatic compounds is the trigonal hybridization sp^2. In contrast to sp^3 form, only three electrons recombine and one $2p_z$ orbital remains unhybridized, often called free or delocalized orbital (Fig. 1.1).

1.1.2 Graphitic compounds

Some of the carbon allotropes, for example diamond and graphite, are well known and commonly used in industry or even in our everyday life. Despite the fact that they are composed from the same carbon atoms, their properties differ significantly. For instance, diamond is hard and optically transparent in visible spectrum. On the contrary, graphite is opaque and soft enough to be used in pencils. As it was mentioned in the previous section, this is caused by different hybridizations of carbon electron orbitals, resulting in distinct atomic structure.

Low dimensional carbon structures have a great importance and they have been studied extensively. One of the first carbon nanostructures, discovered in 1985, was the fullerene molecule (C_{60}: Kroto *et al.*[11]) and later in 1991, carbon nanotubes (Iijima [12]). Arguably, the most significant was the discovery of graphene in 2004 [1]. Since then, the number of publications on this topic skyrocketed and also

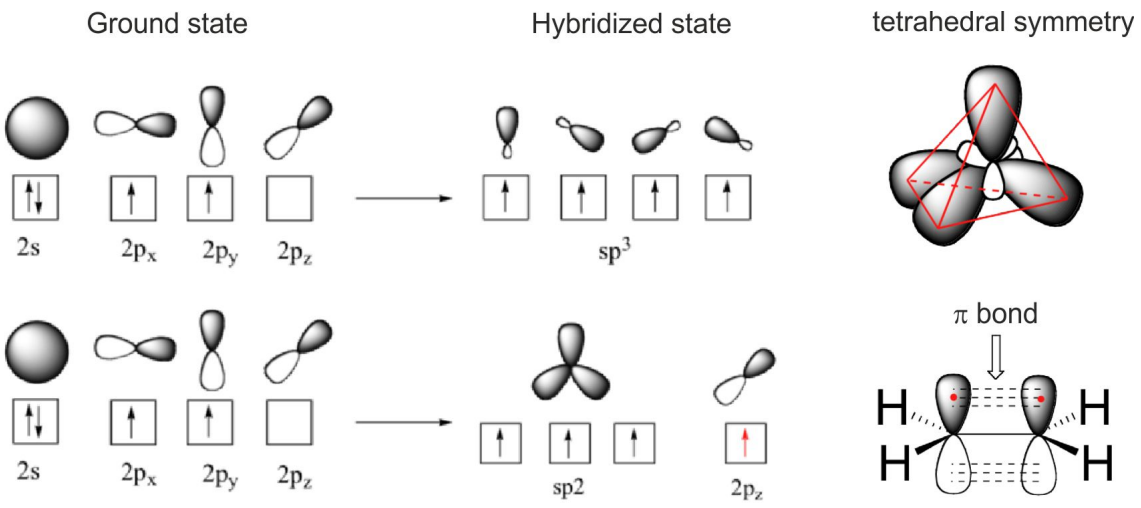

Fig. 1.1: Illustration of hybridization of carbon atom electron orbitals. Hybridized state sp^3, depicted in the upper row, results in tetrahedral symmetry of electron orbitals (e.g. bonding in methane molecule). In the lower row, we illustrate formation of sp^2 hybridization, which combines three of carbon electrons and leaves one unhybridized $2p_z$ orbital. This allows formation of the second asymmetrical π - bond as shown for ethylene. Adapted from [10].

prompted studies of similar 2D materials, e.g. hexagonal boron nitride or silicene. Additionally, the new carbon allotropes were also discovered, e.g. graphane [13] (fully hydrogenated form of graphene) or theoretically proposed penta-graphene [14]. All of the mentioned low-dimensional forms of carbon, together with diamonoids and graphane are depicted in Fig. 1.2.

This master thesis is mainly focused on two dimensional crystal structure of carbon, graphene, which is also illustrated in the Fig. 1.2. There are many descriptions of the graphene layer that help us to visualize it, e.g. the honeycomb like hexagonal structure, the single atomic layer of graphite or the unfold carbon nanotube. Carbon atoms in the graphene layer are hybridized in sp^2 configuration and form covalent σ - bonds with each other. Strong σ - bonds in the horizontal plane are responsible for an extraordinary mechanical properties of graphene, which will be described in section 3.1.1. The leftover $2p_z$ electrons are forming a delocalized $\pi\,(\pi^*)$ - bond and give rise to many of the graphene unique electron properties, discussed in detail in reference [16].

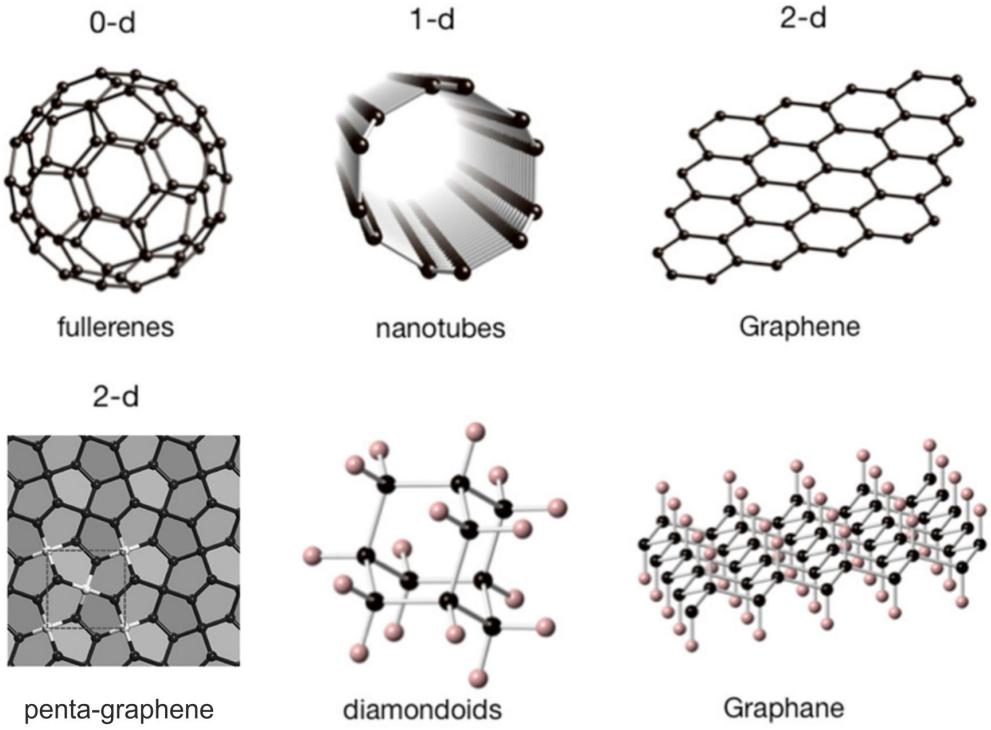

Fig. 1.2: Dimensionality and bonding geometry for different carbon allotropes: fullerene (C_{60}), nanotubes, graphene, diamondoid (admantane) and graphane. The black and off-white spheres represent carbon and hydrogen, respectively. Penta-graphene atomic configuration is isllustrated from top view and the square marked by dashed lines denotes a unit cell. Adapted from [15] and [14].

1.2 Band structure of graphene

Surprisingly, the graphene band structure was for the first time calculated by P. Wallace in 1947 [17]! In his article, he used graphene as a basic structure for calculating electronic properties of graphite, utilizing the tight binding model. Depicted in the Fig. 1.3 is the band structure for graphene hexagonal Brillouin zone. The valence band with lover energy (π - bond) and conduction band with higher energy (π^* - bond) are connected at the charge neutrality points, also called Dirac points (**K** and **K'**)[1]. This makes graphene a unique combination of semiconductor (density of states) and a metal (no band gap). It may be interesting to observe development of electronic structure from single layer graphene to bulk graphite, which is a semimetal. Double layer of graphene exhibits a small band overlap of 0.16 meV [18]. However, the properties of such a structure will be very similar to the single layer, which is advantageously exploited in many applications. With increasing number of

[1]Other meeting points, visible in Fig. 1.3, are equivalent through translation by a reciprocal lattice vector.

graphene layers, the band overlap is rapidly growing. For eleven layers, the overlap is almost the same as in the case of graphite (41 meV). These calculations were also performed using the tight binding model.

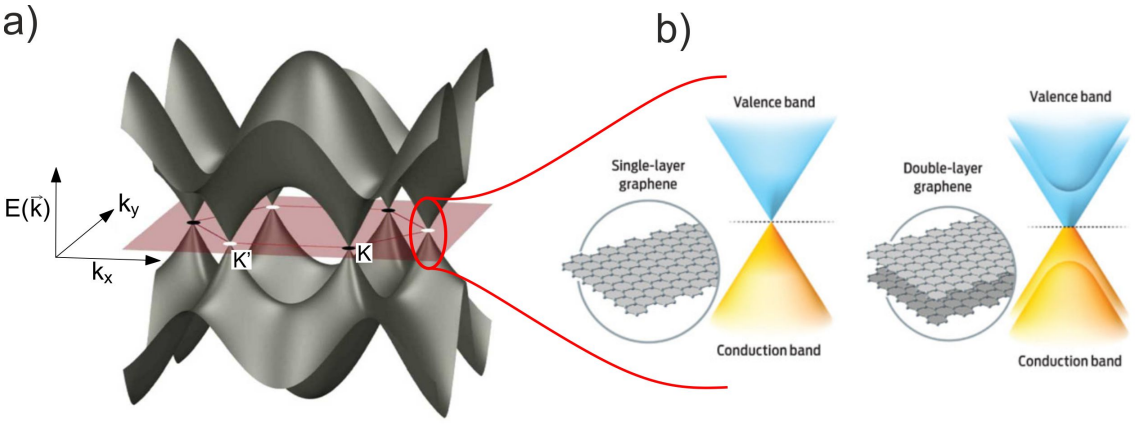

Fig. 1.3: a) 3D illustration of the graphene band structure showing the conduction and valence band, connected at the Dirac points (**K** and **K'**). b) The band structure of graphene near the Dirac points for monolayer and double layer graphene. The linear dispersion relation is similar with massless relativistic particles. In double layer graphene, the overlap of conduction and valence band occurs, but the linearity is partially retained. Adapted from [19] and [20].

One of the most interesting aspects of graphene is the almost linear dispersion relation in proximity of the Dirac point, which can be expressed as [2]

$$E(k) \approx \pm \hbar \nu_{\mathrm{F}} |\mathbf{k} - \mathbf{K}|, \tag{1.1}$$

where $\hbar$ is the reduced Planck constant, ν_F is the Fermi velocity, and $\mathbf{k}$ is a reciprocal lattice vector. Furthermore, if we recall an energy-momentum dependence of a relativistic particle, which reads $E = \sqrt{m_0^2 c^4 + \hbar^2 |\mathbf{k}|^2 c^2}$, and compare it with Eq. 1.1, it may be rewritten as:

$$E(k) \approx \pm \sqrt{m_0^2 \nu_{\mathrm{F}}^4 + \hbar^2 |\mathbf{k} - \mathbf{K}|^2 \nu_{\mathrm{F}}^2}\Big|_{m_0=0}, \tag{1.2}$$

where m_0 is rest mass of particles. One can see that the electrons in graphene can be described as relativistic massless charged particles moving at the Fermi velocity ($\approx 10^6\,\mathrm{ms}^{-1}$) [2]. The charge carriers in graphene can be effectively describe with the Dirac equation for fermions. Consequently the **K** and **K'** points in reciprocal space are denoted as the Dirac points. As the description of the charge carrier properties relies on quantum theory, many unusual phenomena may be observed in graphene. Additionally, the electrons in graphene can be affected by the magnetic field, which leads to new physical effects, e.g. the anomalous integer quantum Hall effect (IQHE) [21].

2 TRANSPORT PROPERTIES OF GRAPHENE LAYER

Deep understanding of graphene electronic transport properties is crucial for its future applications in electronic devices. In reality, it is very difficult to fabricate an ideal graphene structure and one has to deal with deteriorating effects e.g.: defects or contamination from surrounding environment. In this chapter, I will introduce the main parameter for characterisation of graphene layer quality, charge carrier mobility. The most common setups for the mobility measurement will be described as well. In the following sections, I will also discuss the types of scattering effects occurring in graphene layers and the possibilities of their elimination.

2.1 Charge carrier mobility

From solid state physics, it is known that the electrons in a crystal are scattered (by impurities, phonons, or other electrons), therefore they inherent Bloch oscillations[1] are interrupted before their cycle may be completed. The Drude model of electrical conductivity assumes that the electrons can be approximated as free particles, moving in a fixed array of heavy ions, acting as scattering centres. Additionally, interactions between electrons can be included through effective mass. One of the results of this theory is the linear relation between the current density $\mathbf{j}$ and the electric field $\mathbf{E}$

$$\mathbf{j} = \sigma \, \mathbf{E}, \tag{2.1}$$

where σ is the electrical conductivity. For metals, the conductivity is further defined as

$$\sigma = \frac{1}{\rho} = \frac{n \, e^2 \, \tau}{m^*}, \tag{2.2}$$

where τ is the relaxation time, m^* is effective mass of a charge carrier, e is the elementary charge and n is the charge carrier concentration. However, for materials as semiconductors, and also for graphene, where the change of the charge carrier concentration affects the conductivity, it is necessary to define special quantities. This is done by introducing the charge carrier mobility (μ), the ratio of carrier drift velocity (v_d) to the applied electrical field ($\mathbf{E}$).The current density will be then defined as

$$\mathbf{j} = n \, e \, \mathbf{v}_\mathrm{d} = n \, e \, \mu \, \mathbf{E}. \tag{2.3}$$

[1]Oscillation of a particle (e.g. an electron) confined in a periodic potential induced by the electric field.

By combining the equations (2.1) and (2.3) we can see that the conductivity is related to the mobility as:

$$\sigma = n\, e\, \mu \tag{2.4}$$

To a certain extend, we can say that the charge carrier mobility dictates the limiting speed (frequency), at which the device can operate. Additionally, it carries the information about the particle collisions and therefore the energy losses in the material. This directly affects the efficiency of the device.

2.1.1 Field effect mobility

The simplest configuration, commonly used in early experiments with graphene, is field effect transistor (G-FET), described in Fig. 2.1. The advantage is that only two electrodes have to be fabricated on the sample. The third electrode is usually the strongly doped silicon substrate, acting as a back gate with applied voltage V_{G}. A graphene structure is placed on top of insulating layer (SiO_2) with the thickness d. The usual thickness of SiO_2, at which the optimal contrast for graphene occurs, is 280 nm [22]. This structure can be approximated as a plate capacitor with capacitance

$$C = \frac{Q}{V_{\mathrm{G}}} = \frac{n\, e\, A}{V_{\mathrm{G}}} = \frac{\varepsilon_0\, \varepsilon A}{d}, \tag{2.5}$$

where ε is relative permittivity of the material between the plates (SiO_2), ε_0 is the permittivity of vacuum, Q is the charge concentrated on the plates and A is surface of the capacitor plates (graphene layer). The charge carrier concentration can be further expressed as

$$n = \frac{\varepsilon_0\, \varepsilon V_{\mathrm{G}}}{d\, e}. \tag{2.6}$$

By combining equations (2.6) and (2.4), the conductivity of the layer (which is directly measured) is linked with the charge carrier mobility:

$$\sigma = \left(\frac{\varepsilon_0\, \varepsilon\, \mu_{\mathrm{FE}}}{d}\right) V_{\mathrm{G}} = \alpha\, V_{\mathrm{G}}. \tag{2.7}$$

This means that the field effect mobility μ_{FE} can be extracted from the conductivity dependence on gate voltage.

In case of graphene, it holds that by applying the gate voltage we are changing the charge carrier concentration. This causes the Fermi energy level shift around the Dirac point (2.1). When the Fermi level is approaching the Dirac point less states are available for the charge carriers and therefore, the conductivity is decreasing[2]. Further, the change in the charge carrier concentration results in a transitions between the opposite types of semiconductors (i.e. from p-type to n-type) by changing

[2] In fact, for ideal graphene it reaches the minimal conductivity value.

the dominant charge carriers (i.e. from electrons to holes). This is one of the most important characteristics of graphene called ambipolarity [23].

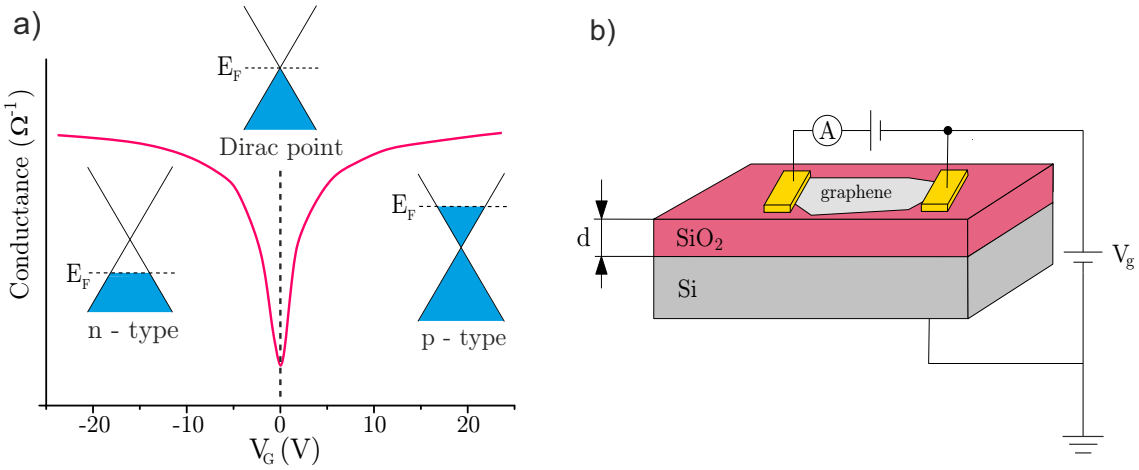

Fig. 2.1: a) Illustration of graphene conductivity dependence on the gate voltage. By modulating the applied voltage, the charge carrier concentration is changing and shifting the Fermi level in graphene. b) A scheme of measurement in field effect configuration.

The position of the Dirac point, which corresponds to the minimum of conductivity in Fig. 2.1, is at 0 V for ideal graphene. In real devices, the Dirac point may be shifted due to the additional doping from substrate, the chemical residues from manufacturing process and can also be strongly affected by molecules in air. This can have negative effect for some applications, but it is also the main advantage of graphene utilization as sensors. It has been shown that graphene can be used for detecting single gas molecule adsorbing on the graphene surface [24].

In contrast to Eg. (2.6), actual value of the charge carrier concentration in graphene can be determined as

$$n = \frac{\varepsilon_0 \, \varepsilon}{d \, e}(V_\mathrm{G} - V_\mathrm{D}), \tag{2.8}$$

where V_D is a value of the gate voltage for minimal conductivity. It is important to mention that the introduced parallel–plate capacitor approximation is valid only when the lateral size of the graphene layer is much larger than a thickness of the dielectric material d.

2.1.2 Hall mobility

An alternative technique to determine the charge carrier mobility is based on determining the charge carrier concentration from the Hall effect. During the measurement of resistivity (DC current flow), the external magnetic field is applied. The

charge carriers then experience the Lorentz force acting on them and influencing their trajectories. Direction of the force is perpendicular to both the charge path (current flow) and the applied magnetic field. A scheme of a typical configuration for measuring graphene field effect transistor, configured in Hall-bar geometry, using low-field magneto-resistance measurements, is shown in Fig. 2.2a. A low out-of-plane magnetic field (B_z) is applied to the sample and the Hall voltage (V_{xy}) is recorded. Then the transverse resistivity of the sample (ρ_{xy}) is calculated as [25]

$$\rho_{xy} = \frac{V_{xy}}{I_{xx}}, \tag{2.9}$$

where I_{xx} is the applied longitudinal current. The charge carrier density can be further calculated from the principle of the Hall effect using the expression

$$n = \frac{B_z}{\rho_{xy}\, e}. \tag{2.10}$$

The charge carrier concentration is tuned by applying the back gate voltage (V_G) similarly as in previous section about FET configuration (2.1.1). However, by using this approach, it is not necessary to approximate the value of charge carrier concentration from parallel-plate capacitor model.

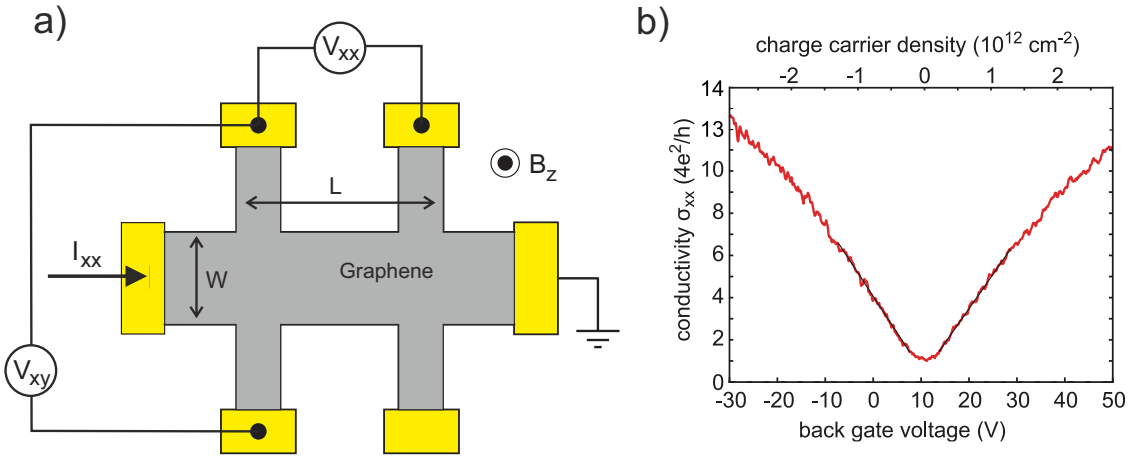

Fig. 2.2: a) Schematics of a measurement in Hall bar configuration. b) Longitudinal conductivity of graphene layer measured as a function of the back gate voltage (for temperature of 2 K). The Dirac point is observable around $V_G \simeq 10\,V$. Adapted from [26].

Next step for determination of the mobility is to calculate the longitudinal resistivity of the graphene layer

$$\rho_{xx} = \left(\frac{W}{L}\right)\left(\frac{V_{xx}}{I_{xx}}\right), \tag{2.11}$$

where W and L are width and length of the layer, respectively. Finally, the charge carrier mobility (Hall mobility) is calculated as:

$$\mu_H = \left(\frac{1}{n\,e}\right)\left(\frac{1}{\rho_{xx}}\right) = \left(\frac{1}{n\,e}\right)\sigma_{xx} \tag{2.12}$$

Previous equations hold only for low applied magnetic fields. However, if higher magnetic field is used, classical regime is no longer valid and it is possible to observe physical phenomena as Shubnikov–de Haas oscillations of σ_{xx} or Quantum Hall effect [2] in the graphene layer.

2.2 Scattering in graphene

This section contains a short overview of several scattering mechanisms exhibited in graphene. Origin of scattering can be found in the graphene layer itself, e.g. due to crystal lattice defects, grain boundaries, or phonon scattering. The most prominent external sources are charged impurities (Coulomb scattering) confined in the supporting substrate, or residues present on the graphene surface.

2.2.1 Coulomb scattering

Coulomb scattering is a long-range scattering mechanism, which can be explained in simplified terms as collisions of the charge carriers with a charged impurities. The Coulomb scattering mechanism was one of the first explanations for graphene transport properties [27]. The graphene charge carriers are confined to a plane of atomic thickness, therefore any charged impurities (e.g. ions, molecules) in their surrounding can strongly influence the conductivity of the layer. Change in graphene conductivity can be approximately calculated as

$$\sigma(n) = C\,e\left(\frac{n}{n_{\mathrm{imp}}}\right) + \sigma_{\mathrm{res}} \tag{2.13}$$

where n_{imp} is the concentration of the charged impurities, σ_{res} is residual conductivity at $n = 0$ and C is a general constant. Results of the experiment shown in Fig. 2.3 are confirming this dependence. Density of the charged impurities in graphene was increased by the deposition of potassium atoms onto a clean graphene surface in ultrahigh vacuum [28]. The calculated value of constant $C = 5 \times 10^{15}\,\mathrm{V^{-1}s^{-1}}$, was in excellent agreement with theoretically determined value. A theoretical model was also developed for the routinely used devices with graphene deposited on SiO_2 [29]. The charged impurities are assumed to be trapped in SiO_2 layer and their concentration is a parameter in calculations of the fit ($n_{\mathrm{imp}} \sim 2 - 4 \times 10^{12}\,\mathrm{cm^{-2}}$). Most of observable features of graphene at zero magnetic field were explained by

employing the Boltzmann kinetic equation with the random phase approximation. However, it is not completely verified if the impurities are trapped in the substrates. Similar values of mobility in suspended and supported graphene (before annealing[3]) suggest possibility of trapped charges in residues between the substrate and graphene or on top of the graphene layer [7].

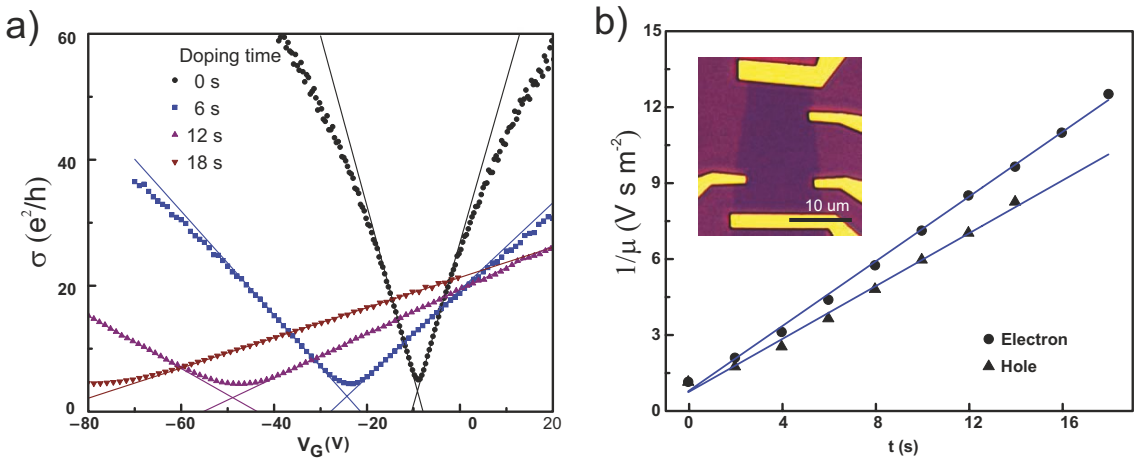

Fig. 2.3: a) The conductivity σ versus the gate voltage (V_G) for the pristine sample and three different doping concentrations of graphene taken at 20 K in UHV. b) Inverse of electron mobility and hole mobility versus doping time. Inset picture shows an optical image of graphene layer with five golden electrodes used for the measurments. Adapted from [28].

2.2.2 Lattice disorder scattering

Crystal defects of the ideal graphene layer, shown in Fig. 2.4 a, can be divided into three basic classes: point defects, line defects and grain boundaries. Point defects include rotation of one carbon-carbon bond and creation of one hepta- and one pentagon, known as the Stone-Wales defect, which is depicted in Fig. 2.4 b. Atomic vacancies can also occur, one- and two-atom vacancies are shown in Fig.2.4c,d. If two atoms are missing, the binding energy increases, because the crystal structure can reconfigure to one octagon and two pentagons. Further recombination of point defect leads to creation of more energetically stable line defects and consequentially the grain boundaries. Effects of various lattice disorders on charge scattering differ, and are still argued in literature. Review on this topic can be found in reference [30].

Graphene fabricated by the chemical vapour deposition, used in this thesis, has strong polycrystalline character. Studies of the grain boundaries suggest limiting

[3]Form of graphene cleaning.

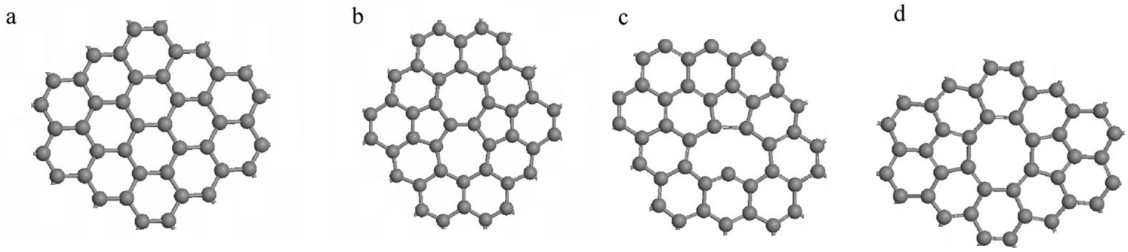

Fig. 2.4: Defects of the graphene crystal structure: a) ideal graphene, b) the Stones-Wales defect, c) one atom vacancy, d) two atom vacancy. Adapted from [31].

influence on the charge carrier mobility (e.g. [32]). Some theoretical models predict formation of localized states near the charge neutrality point. These states could resonantly scatter charge carriers in graphene and give rise to the conductivity with linear dependency on charge concentration. This behaviour is therefore similar to effect of Coulomb scattering and was observed for scattering at grain boundaries [33].

2.2.3 Electron–phonon scattering

Atomic bonds in a crystal can be approximated as springs. Therefore, atoms are forced to oscillate (vibrate) in collective excitations called phonons. The periodicity of the lattice means that phonons have band structure in much the same way as electrons and therefore can interact at many different energy levels. The lattice vibrations are intrinsic scattering source, i.e., they limit the mobility at finite temperatures, when other scattering sources are removed. However, electron-phonon scattering in graphene and its bilayer was estimated to be so weak that, if the extrinsic scattering sources are eliminated, room temperature mobilities can reach values up to $\sim 200\,000\,\mathrm{cm^2V^{-1}s^{-1}}$ [34]. This value exceeds natural mobility of any other semiconductor. In Fig. 2.5 b, the theoretical evolution of mobility for different charge concentrations is shown. In this case, the calculation considered only the weak deformation potential scattering from the thermal lattice acoustic phonons, which limits the charge carriers mobility. Additionally, the phonons from polar substrate can produce fluctuating electrical fields that scatter the charge carriers in graphene. This is called remote interfacial phonon (RIP) scattering mechanism and it is responsible for additional contribution to resistivity above 200 K [6].

I would end this section with conclusion that the graphene conductivity for temperature below 300 K can usually be described with empirical law $\sigma(V_G, T) = \sigma(V_G) + \sigma(T)$. The linear gate voltage dependence $\sigma(V_G)$ was descried in section 2.2.1. Temperature dependent component $\sigma(T)$ (Fig. 2.5 a), is contributed to

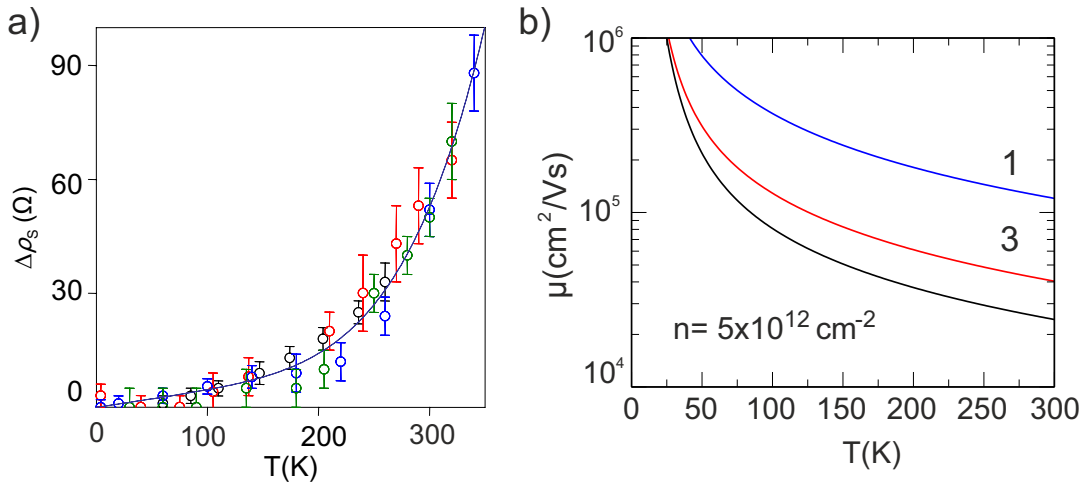

Fig. 2.5: a) The temperature dependent part of resistivity for several single layer graphene samples. b) Mobility limited by the acoustic phonon scattering as a function of temperature for different densities $n = 1 \times 10^{12}, 3 \times 10^{12}$ and $5 \times 10^{12}\,\mathrm{cm}^{-2}$. Adapted from [34] and [35], respectively.

electron-phonon scattering and is unaffected by changes in carrier concentration. Explanations for this addition to conductivity differs in literature and interactions with different types of phonons are considered. I would again referred readers to comprehensive reviews in literature e.g. reference [36].

2.2.4 Increasing charge carrier mobility

A combination of several scattering mechanisms is usually present in real graphene devices. Basically, to increase the charge carrier mobility one have to suppress different types of scatterings simultaneously. For this purpose, several experimental approaches can be effectively used (see review in Ref. [37]).

Graphene is commonly transferred or lithographically patterned by using polymers (e.g. PMMA - Poly(methyl methacrylate)). Even after extensive chemical cleaning, a thin (nm-size) layer or droplets of residues remains on the surface (e.g. [38]). This layer can act as additional adsorption site for gases and contribute to Coulomb scattering in graphene. In the most cases, annealing is utilized as cleaning process to remove the polymers. Annealing is usually performed in vacuum or hydrogen atmosphere (e.g. [39]). Heating temperature is between $300 - 400°\mathrm{C}$ as higher temperature can have negative effect on the graphene electronic properties.

Arguably the biggest influence on graphene is the substrate material. It is affecting the graphene in three main ways:

- inducing Coulomb scattering by trapping charge impurities (sec. 2.2.1)

- causing mechanical deformations of graphene
- creating remote interfacial phonon scattering (sec. 2.2.3)

The most promising substrate material is probably hexagonal Boron Nitrite (hBN). It has less than 2 % lattice mismatch with graphene, low amount of residual charge traps and it is a dielectric material with large band gap ($\sim$ 6 eV). Additionally optical phonon modes of hBN have high energy, therefore, reduce RIP scattering [40]. Devices made from graphene sandwiched between two hBN crystals were reported to have room temperature mobilities $\sim 100\,000\,\mathrm{cm^2V^{-1}s^{-1}}$ [41] similar to the graphene membranes. Additional methods aim to reduce defects and grain boundaries or apply high-κ materials as a substrate to reduce Coulomb interactions. The most extensive method to ensure no substrate influence, is to manufacture suspended graphene device i.e. a graphene membrane.

3 GRAPHENE MEMBRANES

Complexity of manufacturing processes and applications of a final device is fundamentally different for graphene membrane device contacted by electrodes and without them. Therefore, this chapter will be separated into two sections. The first one deals with applications of freestanding membranes followed by the second section devoted to electrically contacted membranes.

3.1 Freestanding graphene membrane

3.1.1 Mechanical properties

One of the first utilization of a freestanding graphene membrane was characterisation of graphene sheet mechanical properties. Using an AFM tip, a load force was applied on small monolayer membranes of approximately 1 µm in radius. Breaking strength of 1770 nN ($42\,\mathrm{Nm}^{-1}$) was recorded [3]. Applying a theoretical model, the in-plane Young modulus of 1 TPa was calculated, establishing graphene as one of the strongest known materials. Dynamic testing also revealed exceptional behaviour after impacts of high velocity projectiles. In these experiments, small silicon spheres were fired on multilayer graphene (MLG) sheets during laser-induced projectile impact test (LIPIT). Discovered penetration energy of MLG was ten times higher than for macroscopic steel sheets [42].

3.1.2 Thermal expansion

Most of materials increase their dimensions with increasing temperature, which is known as positive thermal expansion. In the extreme conditions, this behaviour can lead to significant stress and possible damage of the structure. On the other hand, some materials can compensate thermal expansion and even exhibit negative thermal expansion (NTE) with increasing temperature. Membranes can often exhibit NTE behaviour, probably due to increases in the frequency of out-of-plane soft acoustic phonon mode, when inter-atomic spacing is increased. [43]

Theoretical calculation predicting NTE for graphene were performed by several authors using different methods (e.g. see reference [44]). However, measurement of the graphene membrane thermal expansion cannot be performed by traditional methods such as x-rays or optical interferometry. Temperature-dependent Raman spectroscopy was used to estimate thermal expansion coefficient (TEC) in temperature range between 200 and 400 K. The experiment showed strong temperature dependence, but TEC remained always in negative values. Room temperature value

is estimated to be $\sim -8.0 \pm 0.7 \times 10^{-6}\,\mathrm{K}^{-1}$ [45]. For example glass has a TEC value $\sim 3 \times 10^{-6}\,\mathrm{K}^{-1}$ and steel $\sim 12 \times 10^{-6}\,\mathrm{K}^{-1}$. Freestanding graphene membrane allows more direct approach. In-situ SEM observation of thermal expansion of graphene was performed by Bao et al. [46]. The membrane is pinned by its edges to the substrate. Therefore, during the cooling, when graphene expands, it buckles and sags (Fig. 3.1b). Expansion coefficient can be approximated by measuring the changes in length of the membrane and subtracting the expansion of the silicon substrate (Fig. 3.1 a). Room temperature value is estimated to be $\sim -7.0 \times 10^{-6}\,\mathrm{K}^{-1}$.

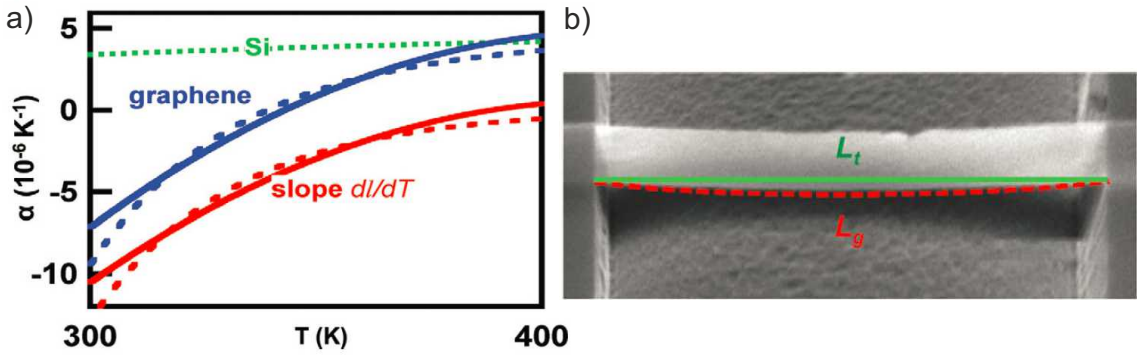

Fig. 3.1: TEC measurement of suspended graphene membrane. a) Determined TEC as function of temperature $\alpha(T)$ for Si substrate (green line) and for the graphene membrane (red line). Their difference is thermal expansion coefficient of graphene (blue line). b) SEM image of a sagging graphene sheet. Adapted from [46].

3.1.3 Graphene as a supporting membrane in TEM

A transmission electron microscope (TEM) is often applied to study graphene structure, defects or growth. On the other hand, graphene itself is an excellent candidate to be used as a supporting material in TEM studies. Traditionally, small samples are placed on supporting grid, but for extremely small samples e.g. bacteria, nanoparticles, utilization of membrane becomes necessary. The objects are normally placed on amorphous carbon or silicon nitride membranes with thickness in tens of nanometres. For specific applications the background noise from these membranes can limit TEM resolution.

Ideal graphene is the thinnest possible membrane but still sufficiently strong to support the specimens, furthermore sp^2 carbon can be considered highly transparent for electrons. Moreover, the periodical hexagonal structure of graphene can be easily filtered out during Fourier reconstruction of TEM images. Individual atoms and molecules on the graphene can be directly observed by conventional TEM. Additionally, real time imaging allows to study dynamics of individual atoms and molecules

[47]. Potential of this application is growing and commercial TEM supporting grids with graphene membranes are already available [48].

Graphene based liquid cell for TEM in situ observation allows to study dynamic growth of nanoparticles. Precursor solution is encapsulated between two layers of graphene, as shown in Fig. 3.2 a, suspended over holes in the conventional TEM grid. Platinum nanocrystal growth was studied in 2012 by Yuk et al. [49]. After locating a liquid pocket in the microscope, the electron beam intensity is modulated to induce the reduction of the Pt liquid precursor, which results in the growth of nanocrystal. Using the aberration corrected TEM they observed crystal-structure evolution with atomic resolution and crystal coalescence processes captured in Fig. 3.2 c,d.

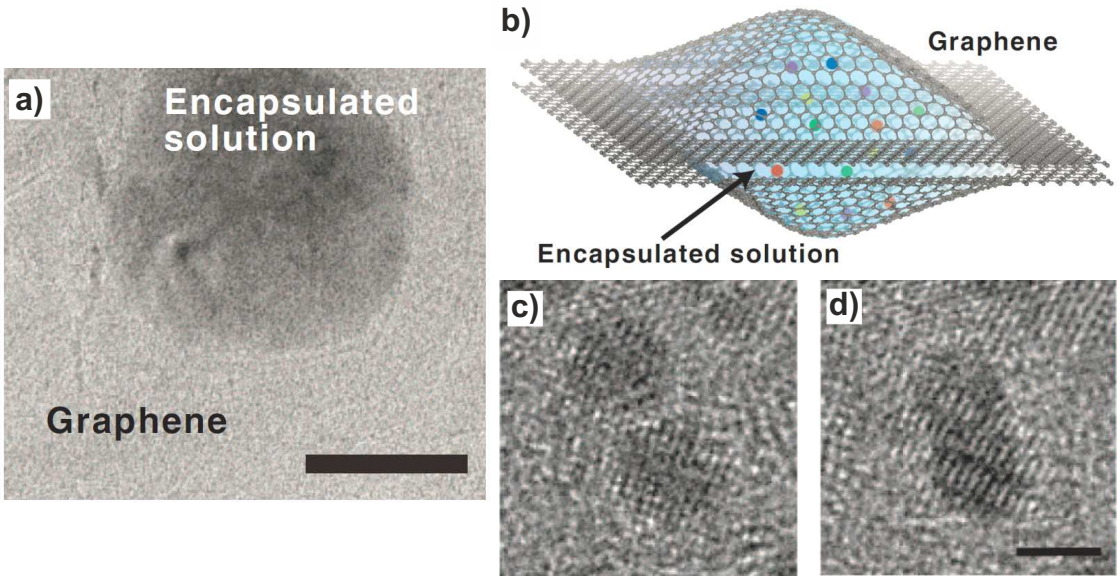

Fig. 3.2: a) TEM image of a graphene liquid cell, Pt growth solution is encapsulated between two laminated graphene layers (scale bar, 50 nm). b) Illustration of the structure observed in TEM image. c, d) Merging of two Pt nanocrystals in solution. Elapsed time between the scans was 2.2 s and the scale bar is 2 nm. Adapted from [49].

3.1.4 Nanoporous membranes

Monolayer graphene membrane is impermeable to standard gases including helium [50]. This attribute itself has many possible applications, such as mentioned graphene liquid cell, discussed in section 3.1.3, or can be used to probe the permeability of gases through atomic vacancies in single layers of atoms. Moreover, controlled patterning of graphene membrane can advance future utilization in molecular filtering.

Sub-nanometre pores in the membrane can be generated and controlled by different methods such as electron or ion beam [51], oxidation or ion/cluster bombardment [52]. Special care must be taken not to compromise essential mechanical properties. Theoretical calculations proved that the nanometre-scale pores in freestanding graphene can effectively filter NaCl salt from water. Reverse osmosis membrane, illustrated in Fig. 3.3, is utilizing high pressure applied to salt water which drives water molecules across the graphene membrane, while salt ions are blocked. Chemical functionalization of the pores with hydrogen can increase water selectivity, whereas functionalization with hydroxyl groups may increase the speed of water transport [53]. Precise membrane perforations and problematic large scale manufacturing are currently limiting this approach to desalination. Recently, the proof of concept measurement was published [54]. Manufactured membrane showed almost total rejection for tested ions (K^+, Na^+, Li^+, Cl^+) and rapid water transport. The flux for pressure driven filtration through the membrane reached value $\sim 10^6 gm^{-2}s^{-1}atm^{-1}$. Graphene oxide based filters are also show some promising results. Review on this topic can be found in reference [55].

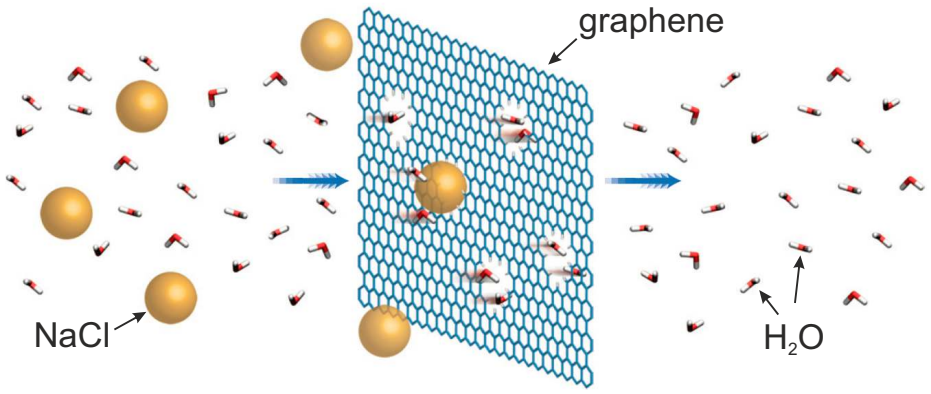

Fig. 3.3: Ilustration of nanoporus graphene membrane filtering salt water. Adapted from [56].

Attractive biological application for graphene nonporous membrane is a single molecule characterisation. DNA and RNA translocation studies have been the focus of many nanopore experiments using biological or Silicon nitride (SiN) membranes.

Device with pores connects two volumes with electrolyte solution and the studied DNA/RNA sequence is added to one of the solutions. Voltage is then applied across the solution to drive the molecules though the pores and ion current is recorded. DNA transitions, shown in Fig. 3.4 a,b, will decrease ion current throughput of the pores. This approach allows to interrogate single molecules and could potentially lead to rapid DNA sequencing. Resolution of the measurement is limited by numbers of nucleotides (DNA base pairs) present in the pore. SiN membranes are usually

tens of nanometres thick, therefore can contain hundreds of nucleotides during each transition. Superior thickness of graphene based device ($< 1\,\mathrm{nm}$) allows only one base pair present inside the pore. [57]

First measurement proving the possibility of the graphene membrane utilization for DNA transition was performed in 2010 [58]. Pores with various diameters were manufactured by highly focused electron beam in TEM. Ten nanometre pore fabricated by this method is shown in Fig. 3.4 d). Transition of single DNA molecule through the pore was recorded as temporary drop in the measured ion conductance. Examples of three different types of transitions for 22 nm wide pore are shown in Fig. 3.4 c, nonfolded (where the molecule translocates in a linear head-to-tail fashion), partially folded (where the molecule is randomly grabbed from the side of the DNA coil, and first translocates in a singly folded fashion), or fully folded molecules (where the DNA happens to be grabbed in the middle of the molecule).

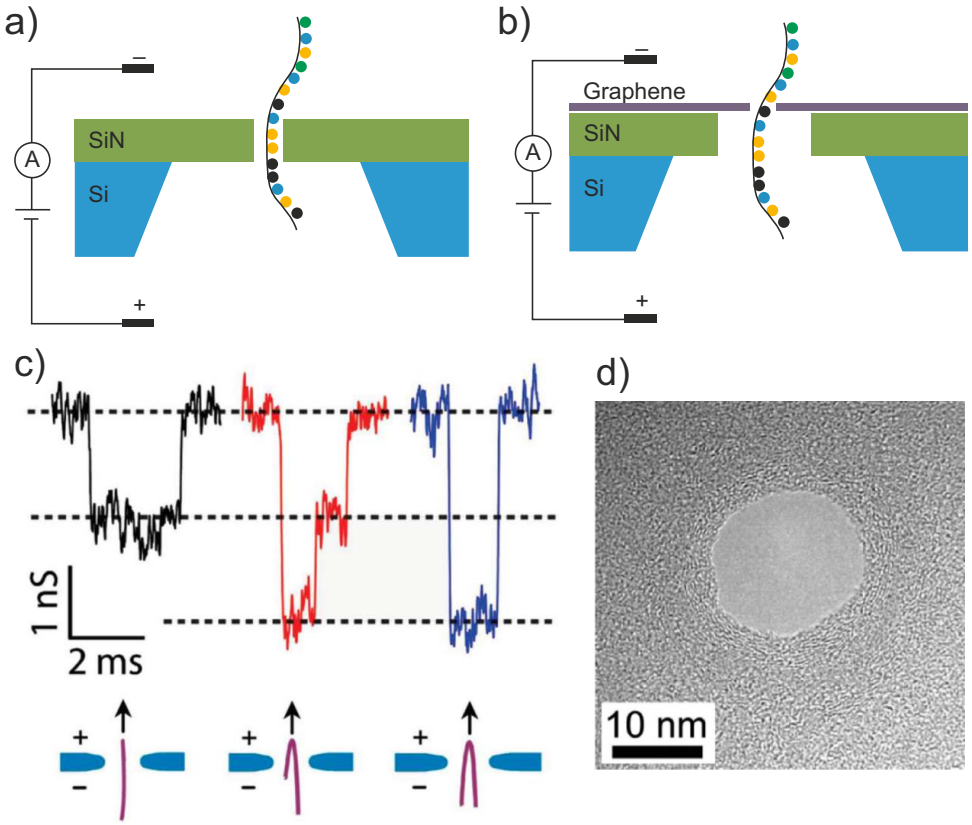

Fig. 3.4: Examples of translocation measurement of RNA for a) SiN membrane and b) graphene membrane. c) Conductance drop during DNA transitions events corresponds to nonfolded (black), partially folded (red), and fully folded molecules (blue). d) TEM image of electron beam drilled pore in graphene membrane. Adapted from [57] and [58].

3.2 Membranes with conductive contacts

3.2.1 Piezoresistive effect

Graphene electrical resistivity can be changed under strain induced structural deformations. This piezoresistive effect together with ability to sustain reversible elastic deformations in excess of 20 % [59] can be used for diverse strain sensing applications [60]. Piezoresistive behaviour in combination with the suspended graphene membrane also allows utilization in the pressure sensing applications.

In principle, the graphene membrane is placed over a cavity etched (or milled) into the substrate with prefabricated electrodes (see Fig. 3.5). The device is then exposed to vacuum environment. Lower pressure outside the cavity causes the graphene membrane to "roll out". The bending or deflection of the membrane is inducing strain inside the graphene layer and it is proportional to pressure difference between air inside the cavity and vacuum outside. [61]

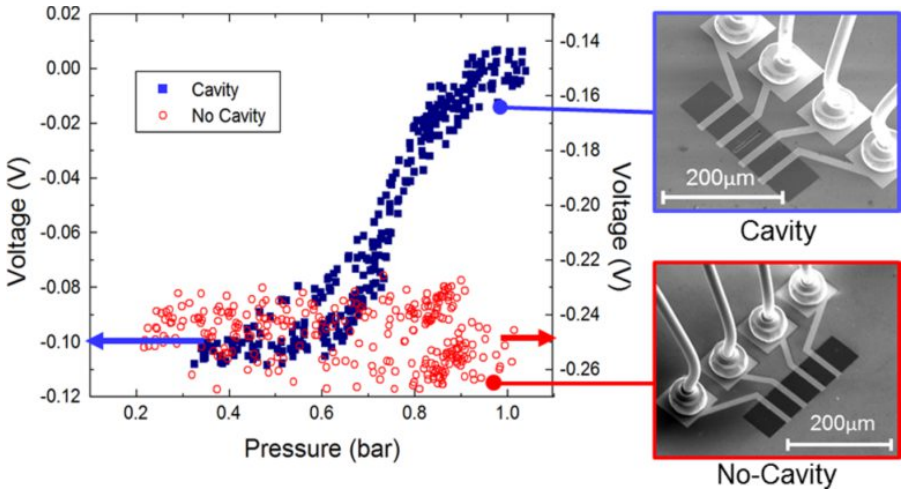

Fig. 3.5: Pressure versus amplified voltage measurements of a device with a cavity (blue squares) and a device without cavity (red hollow circles). Strong dependence can be observed only for the device with a cavity, where the pressure difference leads to bending in the graphene membrane inducing strain and hence changing the resistivity of the graphene layer. Adapted from [62].

Figure 3.5 shows performance of piezoresistive graphene sensor in range of 0.2 to 1 bar. Measured amplified voltage is corresponding to the membrane resistance and is changing with decreasing pressure. Performance of the suspended membrane sensor is compared to the device with identical dimensions fabricated in parallel, but without cavities, in order to verify that strain of the membrane is indeed the underlying sensing mechanism. Calculated sensitivity of the device is 3.95 $\mu V\,V^{-1}\,mmHg^{-1}$.

This value is higher than for conventional piezoresistive Si-based and carbon nanotube pressure sensors. Authors in ref. [62] also argue that when the normalized sensitivity (to the standard membrane area) is taken into consideration the graphene based sensor is 20 to 100 times more sensitive than the conventional sensors.

3.2.2 Mechanical resonators

Behind the NEMS (nanoelectromechanical systems) shortcut is hidden desire to decrease large scale electromechanical devices into the nanoscale. With a decrease in the device size, the sensitivity of sensors, frequency of oscillators, and the packing density of such devices can all increase. Since graphene has unique mechanical properties, briefly discussed in sec. 3.1.1, it is well suited for applications in the NEMS devices. One of the main characteristics of nanoelectromechanical resonators is quality factor, defined as [63]:

$$Q = 2\pi \left(\frac{E_{total}}{\Delta E_{cycle}} \right) = \frac{f}{\Delta f}, \tag{3.1}$$

where f is the resonant frequency of the resonator, Δf is the full width half maximum of the Lorentzian amplitude response peak, E_{total} is the total energy stored in the resonator and ΔE_{cycle} is the energy lost per cycle. For the energy efficient operation, it is desired to have lower energy losses in the system. Additionally, narrower resonant peak means increased sensitivity to changes in resonant frequency, hence, improvement of the quality factor. Many studies for graphene devices created from monolayer or multilayer graphene were published, with Q factors varied in hundreds at room temperature to impressive value of 100 000 at low temperature (90 mK) [64, 65]. For the graphene membrane the damping is found to be strongly dependent on the amplitude of oscillations, which can be described by a nonlinear rather than a traditional linear damping force [64].

The main requirement for oscillating graphene membrane in comparison with the device mentioned in section 3.2.1, is actuating system. The simplest and most used actuation method is probably the application of oscillating voltage to the gate electrode in a field effect transistor configuration. Electrostatic attraction between the gate electrode and the graphene membrane forces the membrane to oscillate (Fig. 3.6 a-inset).

Limiting factor in nanoelectromechanical resonators is motion detection mechanism. It is possible to use interferometric optical method, but this requires sizeable optics setup. For integration purposes the direct electrical readout is necessary. Successfully implemented approach is high-frequency mixing (Fig 3.6 a). R.F. (radio frequency) voltage is applied to the source, at frequency slightly different from actuating frequency f of R.F. gate voltage (V_{g}). Due to the graphene conductance

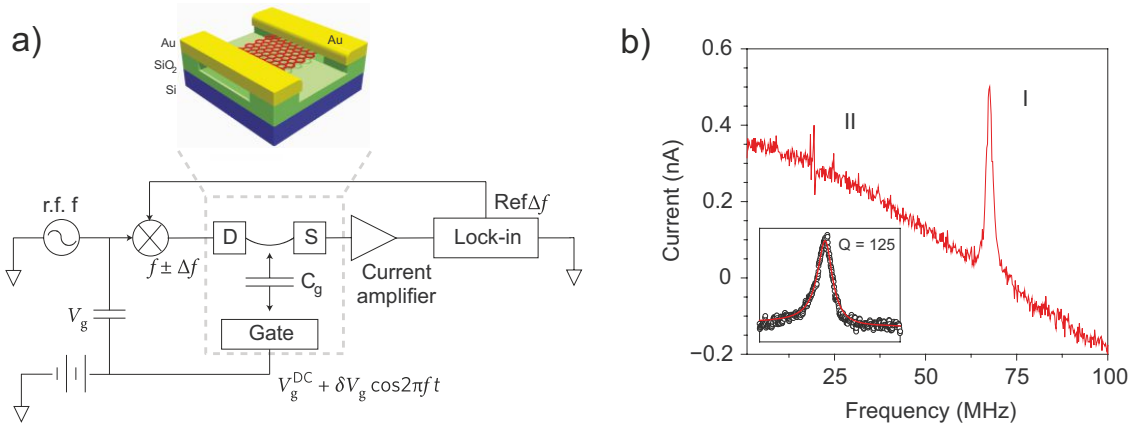

Fig. 3.6: a) A diagram of direct electrical readout of mechanical oscillations in graphene resonator. Gate voltage is applied as a combination of V_g^{DC} and R.F. modulated signal ($\delta V_{\mathrm{g}}^{f}$) used for actuation. Carrier signal is applied to the drain ($\delta V_{\mathrm{SD}}^{f\pm\Delta f}$). The current through graphene is detected by a lock-in amplifier at an intermediate frequency Δf of 1 kHz. b) Detected current ($I^{\Delta f}$) changes with alternating driving frequency (f). Inset shows Lorentzian fit for detected resonance frequency 65 Mhz measured at lower driving amplitude. Calculated quality factor is 125. Adapted from [66].

changes with distance from the gate, motion is detected as a mixed-down current $I^{\Delta f}$ at the different frequency Δf . The frequency response in Fig. 3.6 b shows two most prominent peaks at 25 and 65 MHz, for 1×3 µm monolayer graphene resonator. Smaller peaks were assigned to the resonance of the under-etched gold electrodes. Peak at 65 MHz was interpreted as the mechanical resonance of the graphene membrane. Described devices manufactured by Chen *et al.* [66] also had typical quality factor of 125. Furthermore, resonant frequency of the membrane was observed to be strongly dependent on applied gate voltage ($\mathrm{V_g^{DC}}$). Differences in resonance are also observed with mass changes as was achieved, e.g., by depositing pentacene molecules on the membrane. This could lead to applications in mass detectors.

Similar device was successfully used as replacement for quartz resonators in communication frequency modulators [67]. Frequency of such a device can be electrostatically tuned by as much as 14 %. Device was demonstratively used for modulation of radiofrequency carrier signal for voice transmission ('Gangnam Style' by PSY).

4 FABRICATION PROCESS

The main goal of the experimental work was the fabrication of graphene membrane with conductive contacts. First step was to manufacture a device with two electrodes connecting graphene on Si/SiO_2 substrate, in field effect transistor (FET) configuration, where Si will act as back gate electrode. The optimalization of manufacturing steps would allow to move on to more complicated design with four electrodes and, ideally, Hall bar configuration. This chapter will provide description of fabrication processes with additional general information about methods and used devices.

Fabrication processes of graphene membranes found in literature can be divided into two main categories. First choice is transfer of graphene onto holes or trenches, which are prefabricated on the sample (e.g. by focused ion beam or reactive ion etching). Second one is transfer of the graphene and subsequent removal of the substrate. It was chosen to use the second option in view of two following facts. Large scale CVD graphene was used, which means that further patterning is necessary to create desired shape. Additionally, low mechanical strength of our CVD graphene was previously observed in work of M. Konečný [68]. Therefore, there was a suspicion that patterning of already suspended graphene would rapture the membrane.

Figure 4.1 provides illustration of all manufacturing steps with one exception, graphene fabrication. This process was not done in the framework of this work, but it is described in the first section of this chapter. The sample preparation procedure was designed with regard to possibilities at the Institute of Physical Engineering. Fabrication steps as illustrated are:

1. Deposition (spin-coating) of the PMMA layer for electron beam lithography (EBL), sec. 4.2.1.
2. First EBL procedure to pattern the electrodes, sec.4.2.2.
3. Development of EBL structures in methyl-isobutyl keton solution (MIBK).
4. Deposition of gold by ion beam sputtering (IBS), sec.4.3.
5. Lift-off process (removing the excess gold and PMMA), sec.4.3.
6. Transfer of CVD graphene layer, sec.4.1.1.
7. Cleaning of protective PMMA layer after transfer process.
8. Spin-coating of two layers of PMMA. Protective 50k and standard 495k[1].
9. Second EBL process for patterning the graphene.
10. Development of 2nd EBL structures (in MIBK solution).
11. Removing the excess graphene by oxygen plasma etching.
12. Chemical etching of the substrate by buffered hydrofluoric acid (BHF), sec.4.5. Includes also the most crucial manufacturing step - final drying.

[1] different molecular weight i.e. polymer chain length

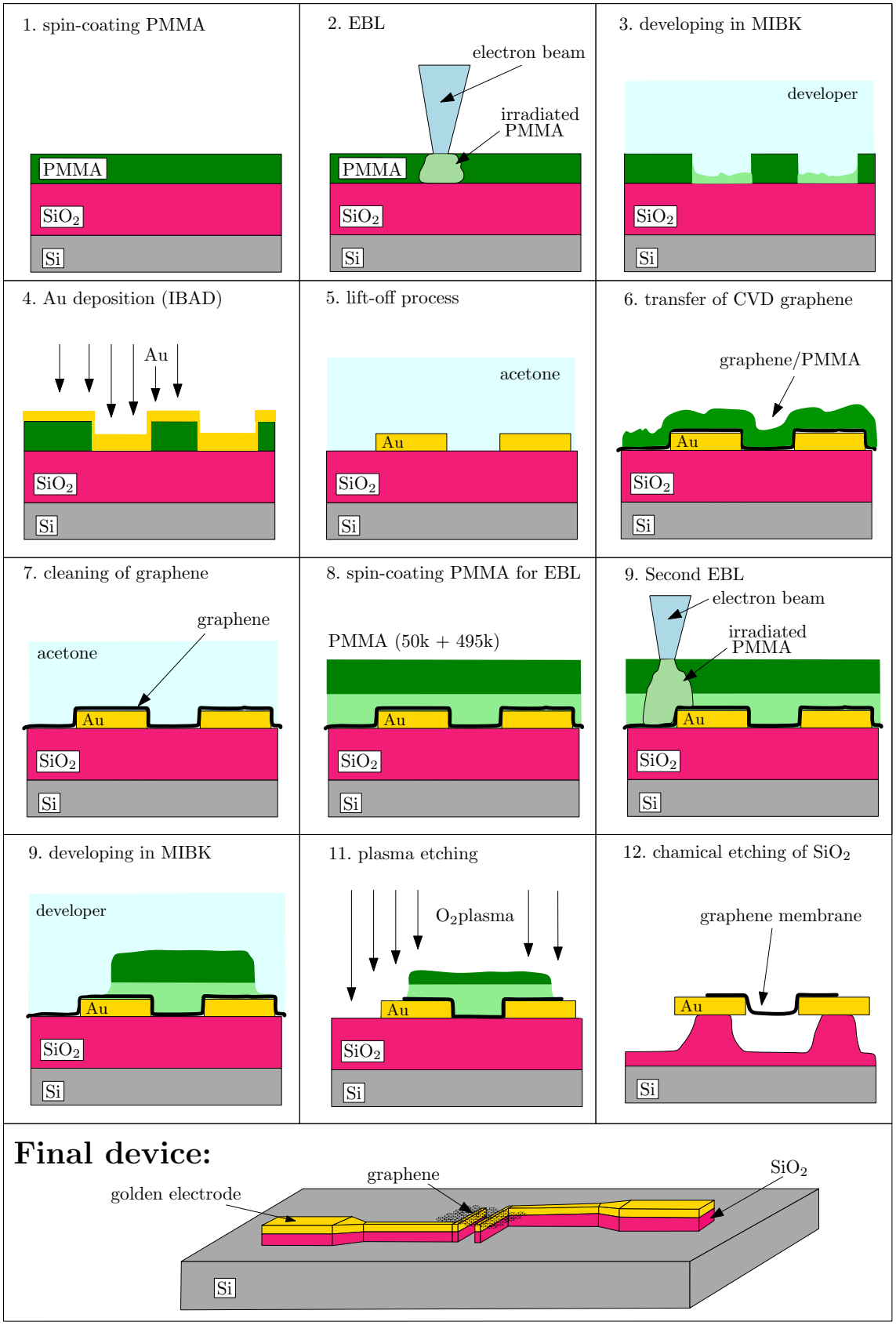

Fig. 4.1: Overview of the graphene membrane fabrication process.

4.1 Graphene fabrication

Graphene layers were manufactured by chemical vapor deposition process (CVD). Usually, a metal foil is heated in the deposition chamber with presence of a short chained hydrocarbon gas molecules (e.g. methane). At a high enough temperature, the gas will thermally decompose to carbon and hydrogen. Metal surface acts as a substrate and also catalyst that reduces the temperature of decomposition ($\sim 1000\,^{\circ}\mathrm{C}$). A promising substrate, also used in this thesis, is copper [69]. One of the advantageous properties of copper is low solubility of carbon, even at high temperatures. Therefore, the growth process is restricted to surface, where decomposed carbon atoms start to nucleate and form the graphene monolayer (Fig. 4.2). This means that the growth process on Cu is self-terminated, since catalytic decomposition will stop after the graphene covers entire surface of copper.

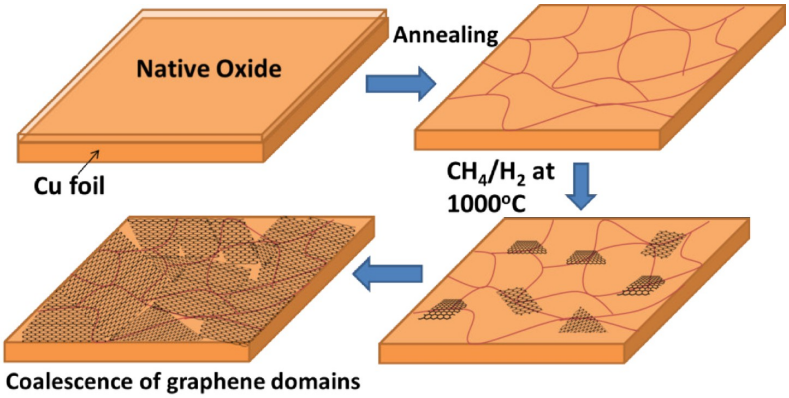

Fig. 4.2: Chemical vapor deposition (CVD) of graphene on a copper substrate. The copper foil is heated up to $1000\,^{\circ}\mathrm{C}$ and exposed to methane gas which is subsequently decomposed on the surface. Than the carbon atoms start to nucleate and grow to form monolayer graphene. Adapted from [70].

Nucleation of graphene starts at many different places simultaneously. Typical nucleation sites are surface impurities, trenches (rough surface) or copper grain boundaries. Graphene individual crystal domains grow from the nucleation centre, until they connect and form a complete monolayer. Therefore, the CVD graphene has a polycrystalline nature. By reducing the number of nucleation sites, it is possible to decrease the density of grain boundaries and improve the quality of the graphene layer. Growth process can be also stopped before the coalescence of domains to obtain single crystal graphene flakes. Utilizing various methods, it is possible to grow graphene single crystals in mm size. Wu *et al.*, for example used electrochemical polishing of copper and high-pressure annealing to achieve graphene crystal size over 2 mm in diameter [71]. Another possibility, developed at

our institute, is to reduce the density of nucleation sites by utilizing ultrasmooth copper foil [72].

Graphene layers used in this thesis were manufactured by Ing. Pavel Procházka, utilizing the deposition chamber designed and fabricated in the framework of his master thesis [73]. Graphene was prepared in quartz crystal furnace on commercial copper foil, 25 µm thick. The foil was heated to 1000 °C and cleaned in H_2 atmosphere at 4 Pa pressure. Growth of graphene was performed with methane precursor gas at 70 Pa for 30 min. Methane flow was 35 sccm.

4.1.1 Transfer process

After the growth procedure is finished, it is usually desired to transfer graphene onto a different substrate (e.g. for analysis). This procedure is illustrated in the Fig.4.3. First the PMMA polymer is spin-coated onto the copper foil with graphene for support and protection. The foil is usually several cm^2 large and therefore is cut into desired size ($\sim 0.25\,cm^2$). Next step is etching of the copper foil. Solution of ferric nitrate ($Fe(NO_3)_3 \cdot 9H_2O$ at concentration $\sim 0,05\,g \cdot ml^{-1}$) was used. Etching time is usually around 12 - 24 h. Graphene/PMMA membrane is then cleaned in deionized water. Membrane is flowing on the water, therefore it is possible to "fished it out" onto the target substrate (prepared sample). Last step is drying and dissolving the PMMA layer in acetone.

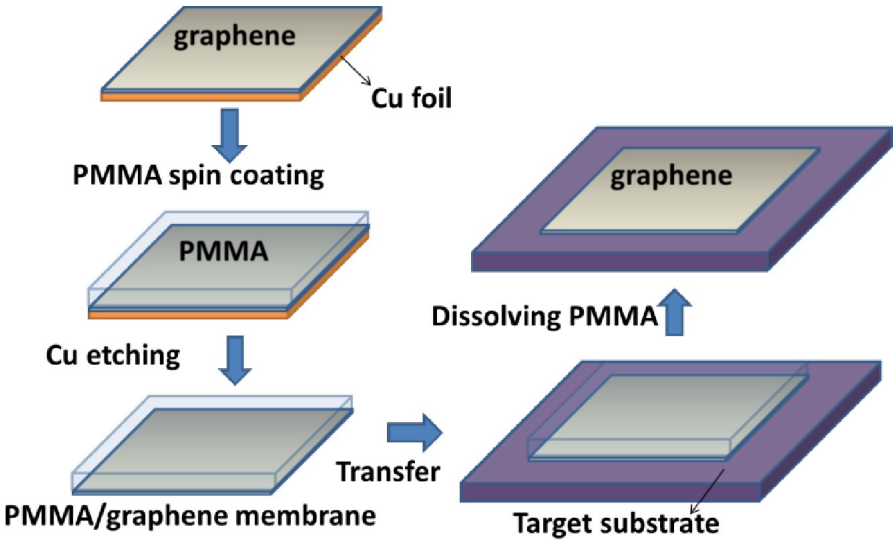

Fig. 4.3: Transfer process of the graphene layer from the copper foil. The PMMA polymer is used as a supporting material. Copper is etched away and the remaining graphene/PMMA membrane is cleaned and transferred on the target substrate. Adapted from [70].

4.2 Electron beam lithography

Principle of electron beam lithography (EBL) is irradiation of electron sensitive material (resist) to create a specific pattern. Accelerated electrons are colliding with resist molecules and locally modify its structure. Depending on the type of the resist, either exposed areas or their surrounding are afterwards dissolved in selective chemical (developer). Lithography process is illustrated in the Fig.4.4. Goal of this section is not to provide a manual for EBL, therefore, only the basic principles will be mentioned. Selected technical information for possible reproduction of this work by experienced users are included. Detailed description of EBL and possibilities of this technique can be found in reference [74]. Additional details of the EBL processes utilized at the Institute of Physical Engineering can be found, e.g. in [75].

4.2.1 Sample preparation

Substrate material is highly p-doped Si (100) with $\sim 280\,\mathrm{nm}$ of thermally grown SiO_2 layer. Silicon oxide provides an insulating layer to separate the top electrode from the back gate (Si). After the cutting of the silicon wafer into the desired size ($1 \times 1\,\mathrm{cm}^2$), it is necessary to clean the surface to achieve better adhesion of the resist. The cleaning procedure consists of putting the samples in an ultrasonic bath for 5 to 10 min in acetone, isopropyl alcohol (IPA) and deionized water, respectively. Further, it is possible to improve the cleaning by including additional steps known from semiconductor industry, e.g. Piranha solution treatment or oxygen plasma.

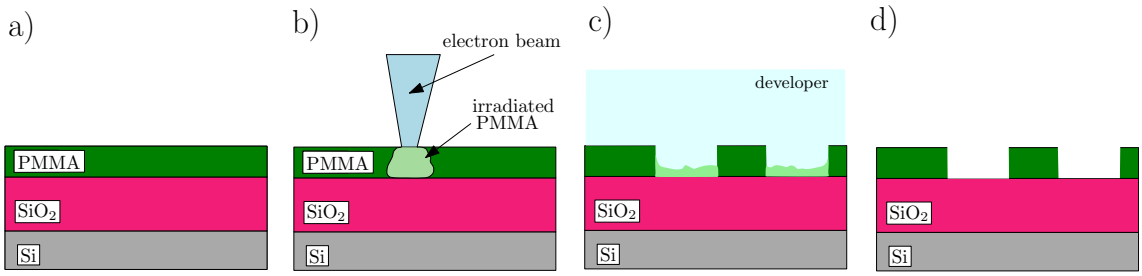

Fig. 4.4: Illustration of the electron beam lithography procedure. a) PMMA resist is spin-coated on the sample, b) designed pattern is created by electron beam, c) irradiated areas of the resist are dissolving in developer (MIBK), d) final structure.

The PMMA polymer was used as the resist material. This material is a rather standard high resolution positive resist. The resist layer is deposited on the sample by spin-coating. The principle is the spinning of the sample at several thousands rotations per minute (rpm) to spread the resist. The faster the rotation is, thinner the layer becomes. Before the spin-coating of PMMA it is recommended to heat

the sample up to 180 °C and keep it at this temperature for several minutes (e.g. 5 min). The previous procedure will induce a desorption of water molecules from surface, which results in further improvement of the adhesion.

The 495k PMMA A5.5 [76] resist was used for the fabrication of the electrodes. The PMMA is dissolved in anisole and has 5.5 % concentration. An additional information is molecular weight as "495k". This means that one chain of PMMA has average molecular weight of 495 000 and it is connected to the length of the chain through weight of PMMA monomer (≈ 100). The spin-coating process consisted from two steps. First the PMMA layer was spread at 800 rpm for 10 s to improve the homogeneity of coverage. Second step determines the thickness and rotation was set to a value of 3000 rpm for 35 s. This process provides a homogeneous layer with thickness of approximately 300 nm. A lower thickness (≈ 200 nm) was used in the first experiments, but it was proved to be insufficient for the lift-off process. Final step after spin-coating was baking for 90 s at 180 °C to harden the layer.

4.2.2 Fabrication of electrodes

A lithography procedure performed using scanning electron microscope (SEM) does not require a mask since the pattern is directly written in to the resist layer. The electron microscope **Lyra 3** manufactured by **TESCAN** was used in this work. It is a dual beam system which combines scanning electron microscopy and focused ion beam. The microscope has fully motorized stage which allows automatic movements during the resist expositions. The Schottky field emission cathode is used as an electron source. For the utilization as an electron lithograph, it is also equipped with beam blanker device, which allows fast deflection of the beam from the sample.

The final design of electrodes for two-point measurements is shown in the Fig.4.5. Maximum of four final devices can be manufactured on one sample. Number is limited by the sample holder designed for electrical measurement (described in sec. 5.1). There are seven fields of smaller electrodes, to utilize the large area of CVD graphene as best as possible. Multiple membranes were manufactured between these smaller electrodes. This will be described in section 4.4 about patterning of the graphene. Afterwards, all damaged membranes or unused electrodes were isolated with focused ion beam.

The design of electrodes was created in the CAD like program **DrawBeam Advanced**, supplied by the manufacturer. Objects can be organized into layers and each layer can have a separate set of parameters. There are four basic parameters: beam current, spot size, dose and spacing. First two parameters can be supplied by a built in simulation software, but it is better to determine the values experimentally. Beam current can be measured by the integrated ammeter. To achieve a

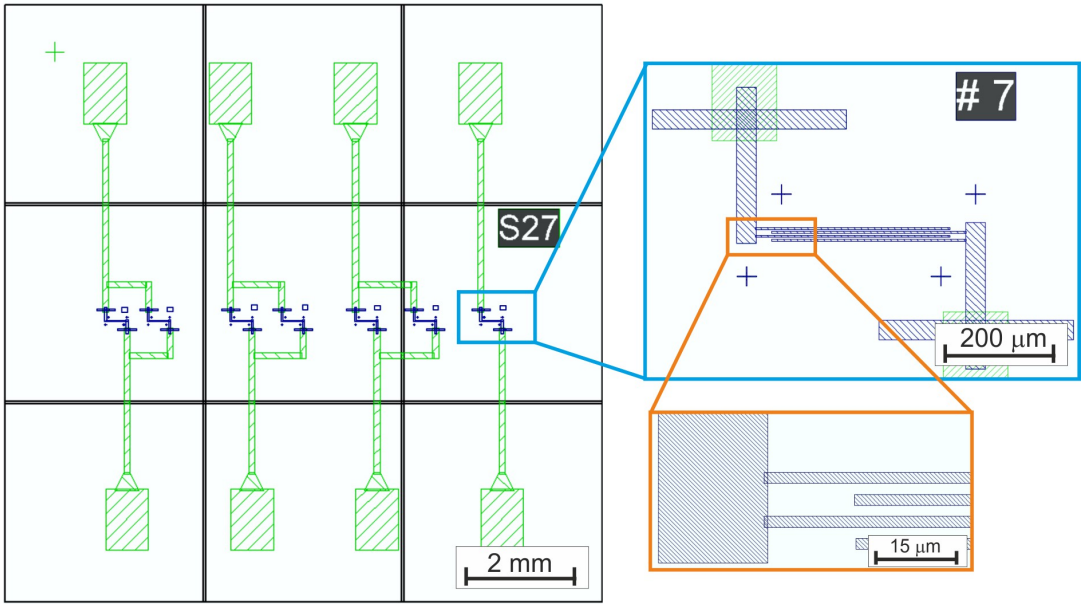

Fig. 4.5: Final design of electrodes for EBL(sample size 1 cm). Structure are colored in green and blue, corresponding to different layers for heigh current and normal lithography process respectively.

precise measurement it is necessary to focus the beam into the Faraday cup, which is essentially only a deep pit fabricated in the sample holder. Beam size is corrected by changing the spacing parameter. Spacing value 1 means that the distance between irradiated points will be exactly the estimated beam diameter. Similarly, if the value is 0.5, the distance will be half of the diameter. Last parameter is dose in $\mu C/cm^2$, which determines, how long will the beam stay over the specific spot (dwelling time). The dose must be sufficient to cause changes in the resist material. In case of the PMMA, electrons are breaking the polymer chains, therefore, the exposed areas are more soluble in the developer than the rest of the PMMA layer.

Exposition settings

Fabricated structures were divided into two groups (layers), which were manufactured by different settings. Blue (finer) structures in Fig. 4.5 were patterned with the beam size of $\sim 100\,nm$ which corresponds to a beam current of approximately 7 nA. Write field was set correspondingly to 1100 µm. This means that the exposition of whole sample was divided into 9×9 separate fields. A motorized stage with the sample automatically moved between the fields. Optimal parameters proved to be dose of $350\,\mu C/cm^2$ and spacing 0.8. Additionally, the structures were arranged so that each group of electrodes in blue layer had a large overlap with electrodes in green layer, as shown in magnified field 7 in Fig. 4.5. This compensate for the

possible misalignment of the two exposition steps.

Exposition of green structures (larger electrodes) with standard procedure would take a significant time (e.g. 1 h for 10 nA current). Therefore, the technique was devised to utilize maximal beam current of the electron microscope. Schottky field emission gun can provide emission of electrons in μA. This value is significantly reduced by column optics to achieve optimal resolution, for Lyra microscope it is ≈ 200 pA to get beam size of ∼ 3 nm at 30 kV accelerating energy. The procedure for increasing the current to its maximum possible value, can be found in the manual of the microscope. Maximum current value can be tuned from 100 nA up to 180 nA, depending on the actual state of calibration and deterioration of the cathode. Several cathode exchange were performed during the span of this thesis, but standard value was usually around 130 nA. On the other hand, the value of 190 nA was also observed. At these electron currents the exposition takes less than 10 min.

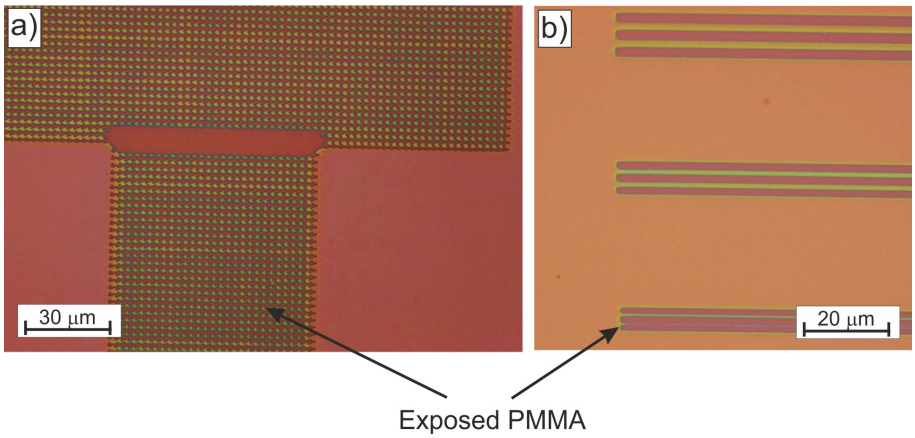

Fig. 4.6: Optical microscope pictures: a) structure with too high spacing parameter, created by HC EBL in Resolution mode, b) resolution test showing structures created in FIELD mode with parameters: spacing 0.8 and dose 300 $\mu C\,cm^{-2}$. Structures are rectangles with 2, 3 and 4 μm width.

The lithography test using high current (HC) has proven to be problematic. The main problem consisted in estimation of the beam spot size. Optical microscope picture (Fig. 4.6 a) shows the result of HC lithography with unsuitable spacing parameter. Even after optimalization of the parameters, the results were often unsatisfactory and with bad resolution (5-10 μm spot size). To improve the resolution a different imaging mode of **LYRA** SEM was utilized. Standard **Resolution** mode was switched to **FIELD** mode. This setup is usually used to gain high depth of focus for imaging of samples with excessive features. In **FIELD** mode the objective lens was switched off and the microscope was utilizing intermediate lens for imaging. Usually it is said that the **FIELD** mode sacrifices the resolution for increase

in depth of focus. This is not true for high currents and spot size $\sim 1\,\mu m$ can be achieved for 130 nA. Resolution test was performed and optimal parameters for this technique were determined as 0.8 spacing and dose $300\,\mu C/cm^2$. Figure 4.6 b shows structures created by HC EBL. The visible lines are designed as rectangles with 2, 3 and 4 μm, separated by the same size gap. It was estimated that for structures as close as 6 μm the proximity effect will be sufficiently low. Therefore, actual size of the electrodes is approximately the same as the designed size.

Actual parameters for HC EBL fabrication of electrodes in the green layer (Fig. 4.5) were higher than the optimal ones. Used values: spacing 0.7 and dose $500\,\mu C/cm^2$. The electrodes had a minimal size of 100 μm, therefore, the resolution of the lithography was not crucial. However, actual reason for increase of the parameters were inhomogeneities in the resist layer (usually on the sample edges). This areas were not sufficiently exposed, because the resist was thicker. Higher dose has not significantly increased the exposition time, but it ensured that the EBL process was almost always successful.

Last step after the exposition of resist is developing (Fig.4.4 c), which consisted of 90 s bath in methyl isobutyl ketone (MIBK) and IPA (1:3) solution. Further, the sample was put in to the IPA solution for 30 s. Isopropyl alcohol dissolves the MIBK and stops the developing process[2]. Final step is rinsing the sample in dionized water.

Length of membrane

Important fabrication parameter is distance between the electrodes, which determines the length of the membranes. The optimized distance of electrodes was between 2 μm and 3 μm. The length of the membrane was presumably limited by elongation after removal of the substrate. The reason for this originates in the fabrication process of graphene, described in the sec. 4.1. During the manufacturing process, the copper substrate covered with graphene, is cooled from $\sim 1000\,^\circ C$ to room temperature. Graphene and copper exhibit different thermal expansion coefficients, therefore the graphene layer is wrinkled. When the graphene layer is transferred on the substrate it retains its shape. After the removal of the substrate the wrinkles can straighten, therefore, the graphene layer will elongate.

First experiments were performed with electrode distances of 20, 15 and 10 μm, all unsuccessful. Graphene layer was in all instances attached to the substrate. Extent of graphene bending, was estimated from a freestanding graphene membrane. The membrane was created by placing CVD graphene on the substrate with prefabricated trenches (Fig.4.7 a). Square trenches were milled into SiO_2 substrate by

[2]IPA solution also develops the PMMA resist but at much slower rate than MIBK.

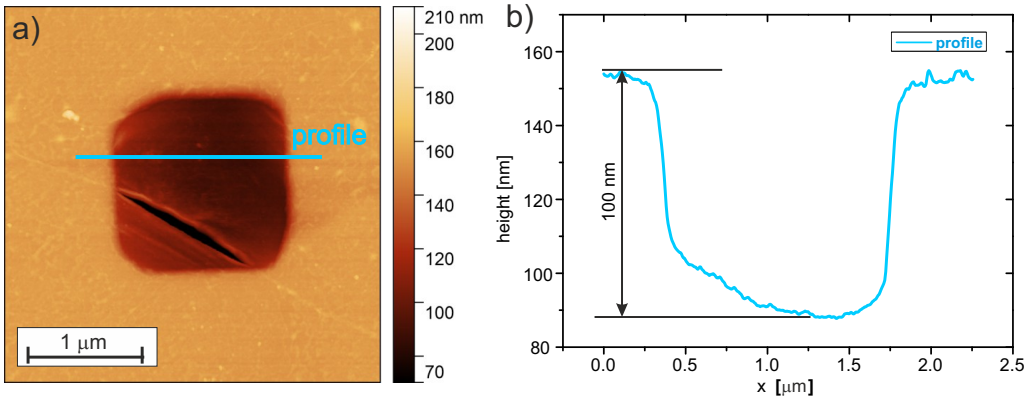

Fig. 4.7: a) AFM topography for 1 µm graphene membrane fabricated by placing CVD graphene on a trench prepared by milling with FIB. b) Profile line showing about 100 nm bending of the membrane.

focused ion beam. The graphene sag was estimated from the AFM measurement to a value of about 100 nm, for membrane size ~ 1.5 µm (Fig.4.7 b).

4.3 Deposition and lift-off

Electrodes on the sample were fabricated by deposition of gold onto prepared EBL structures (Fig. 4.8 a). The procedure was performed with the ion beam sputtering (IBS) apparatus Kauffman at the Institute of Physical Engineering. Device is bombarding a target from the desired material with argon ions, which sputter the material on the samples. Actual deposited layer was combination of 3 nm thick Ti adhesive layer and 97 nm thick golden layer.

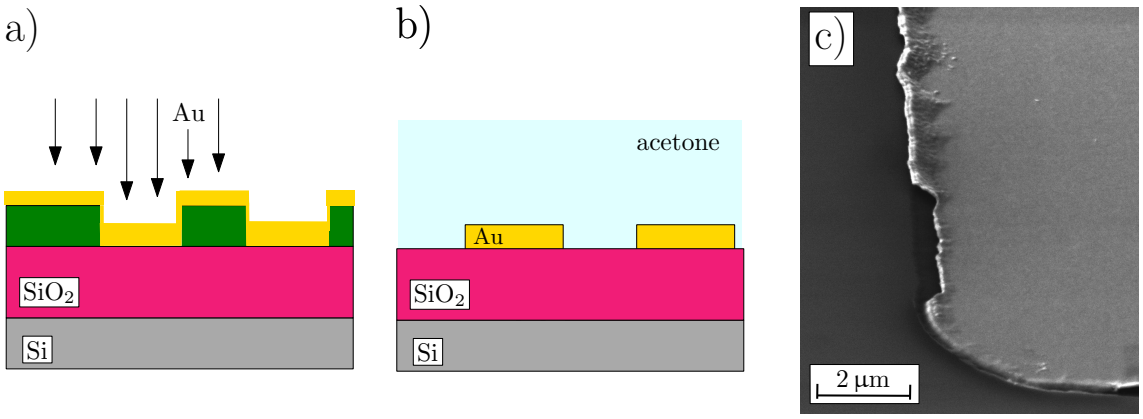

Fig. 4.8: a) illustration of gold deposition by IBS, b) lift-off process c) picture from SEM showing residual gold material on the electrode edges. Gold in SEM appears brighter than Si or SiO_2.

After the deposition, the sample was placed in acetone to dissolve the PMMA. This is called the lift-off process. The goal of this step is to remove all excessive gold from the sample. Ultrasonic bath may be used to improve and speed up the process. It is also possible to heat up the acetone solution, but this must be performed cautiously, since it is a volatile chemical. Residual material can stay on the edges of the electrodes (Fig. 4.8 c). These structure are most prominent in one direction, which is caused by angle of the deposition. It is recommended to take this into consideration when placing the sample in the deposition chamber.

4.4 Patterning the graphene layer

Second lithography step is performed after transfer of the graphene layer on the sample, described in sec. 4.1.1. Transferred graphene was covered by PMMA protective layer. The layer is inhomogeneous and therefore cannot be used for EBL. Instead, the PMMA was cleaned by immersing the sample in acetone solution for 1h. Afterwards, new multilayer is spin-coated on the graphene. For the first layer the 50k A3 PMMA was spread at 4000 rpm creating approximately 80 nm thick layer. The short chained 50k PMMA layer was added to reduce the PMMA residues on the graphene surface after EBL. Second layer was made by A5.5 495k PMMA, spin coated at 3000 rpm ($\approx$ 300 nm).

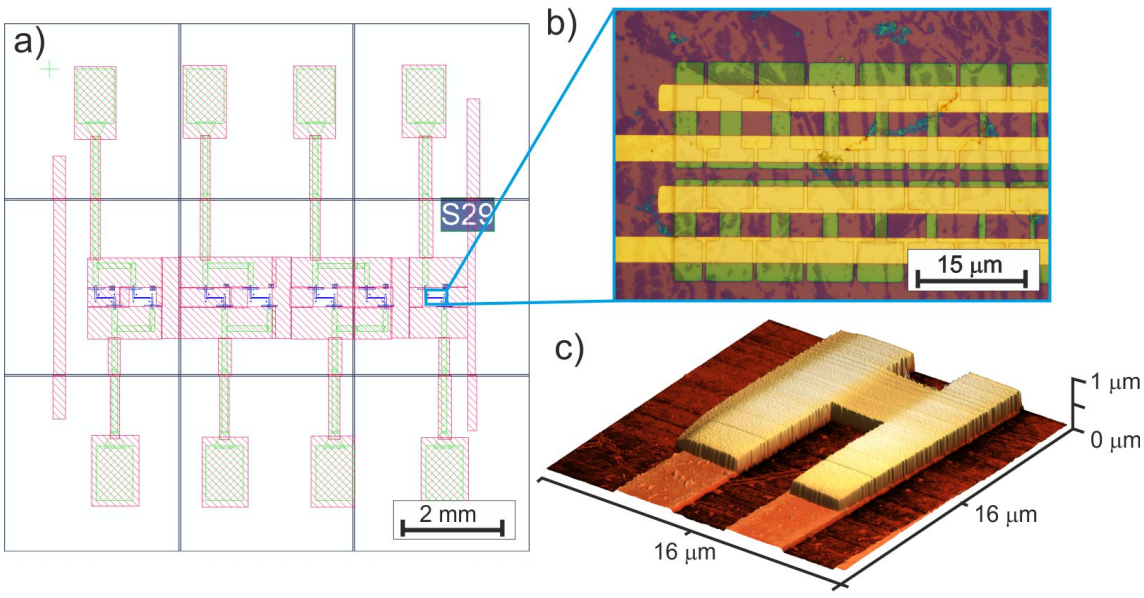

Fig. 4.9: a) EBL structures exported from DrawBeam editor. Surroundings of electrodes (green layer), patterned (red layer) to isolate them from graphene layer. b) Developed pattern of fine structure for plasma etching, imaged in optical microscope. c) 3D AFM topography of single structure for 3 µm membrane.

Exposition was performed manually on each of the seven fields with small electrodes. Precise alignment was achieved by manual alignment procedure on four marks fabricated in the first EBL step (crosses shown in Fig. 4.4). Write field was set to 650 µm, beam spot size was 60 nm corresponding to about 4 nA at 30 kV. Exposition parameters were 350 µC/cm^2 and spacing 0.8.

The pattern created on graphene by EBL and developed in MIBK:IPA solution, is shown in Fig. 4.9. Structures had various widths to test the possible sizes of the graphene membranes. After developing, sample was exposed to oxygen plasma, which removes graphene unprotected by the PMMA layer. Plasma etching was performed in device Resist striper NANO from DIENER. Etching time was 4 min (minimal) at 100 % power and set 0.5 mbar pressure of O_2. Oxygen plasma also removes the PMMA and etching rate was experimentally determined to be 15 nm/min, for 495k PMMA.

The surrounding of the gold electrodes, created in the first EBL step, was also exposed to isolate them from the graphene layer. This ensures that devices in different fields were not connected. Additionally, it minimized the leakage current between the top electrodes and the substrate, because the contact surface was reduced. Pattern created in the DrawBeam program is shown in Fig. 4.9 as red layer. High current EBL was used for the exposition, with the same settings as in the first EBL step, to reduce the fabrication time.

4.5 Chemical etching

Last fabrication process is chemical etching of the SiO_2 substrate, performed by hydrofluoric acid (HF). It is a commonly employed etchant, used in semiconductor industry for removing of the native SiO_2 layer from the silicon surface. Chosen solution is called buffered hydrofluoric acid (BHF), which consisted of 40 % NH_4F and 39 % HF in 7:1 ratio[3]. Role of the buffer, the ammonium fluoride, is to slow the etching process and improve the uniformity of etching. Etching rate can be found in literature (e.g. [77]), but was also determined experimentally to $\sim$ 70 nm/min at 23 °C. It is important to note that etching rate is strongly dependent on temperature.

Complete etching procedure is shown in Fig. 4.10. Sample is etched in BHF solution for 3.5 min for samples with 280 nm thick SiO_2 layers. Afterwards, sample is transferred to deionized water to wash away the BHF. Next steps were aimed to improve the membrane survivability of the fabrication process. The sample was transferred to several solutions of water and isopropyl alcohol (IPA) to gradually

[3]It is the ratio of designated chemicals, which are already solved in water in marked concentration.

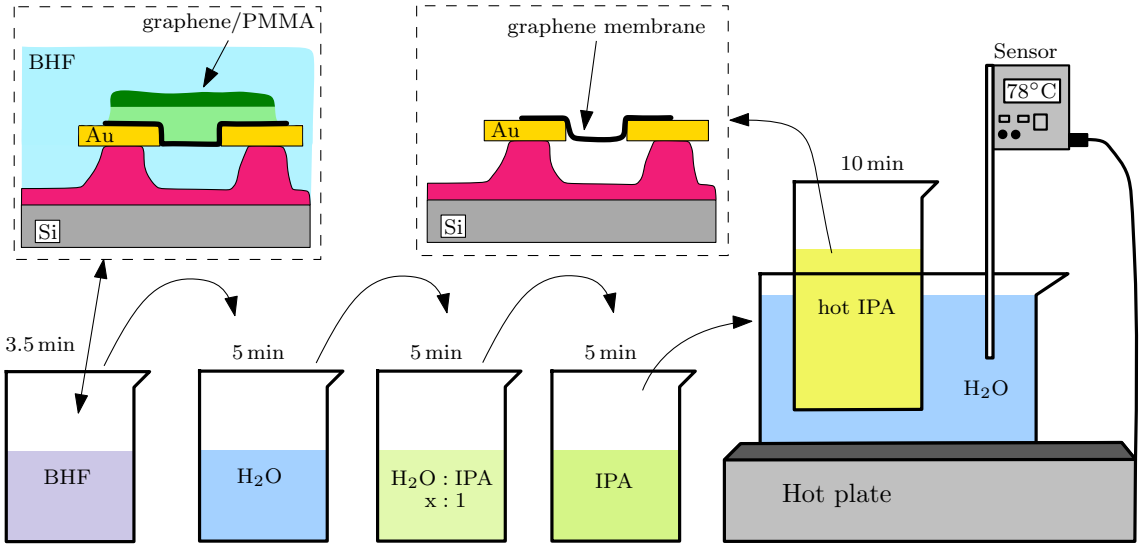

Fig. 4.10: Step by step illustration of the etching process. Several solution of H_2O and IPA were employed with various raptures indicated by the x = 3, 2 and 1.

reduce the surface tension. Optimal final step was determined as immersion in IPA heated to 78 °C. Further explanation for this step is provided in the next section.

4.5.1 Drying

The survivability of the membranes was mostly determined by the drying procedure. During the drying, the surface tension of the liquid is pulling the membrane to the substrate. This will result in creation of a rupture or attachment of the graphene to the substrate [78]. Unsuccessful suspension of the graphene is shown in the Fig. 4.11 a. Two processes can be found in literature to eliminate this influence. One option is to avoid the surface tension from liquid-gas-interfaces by performing the drying at the critical point[4] of the solution. This procedure requires specialized equipment and was used for successful suspension of graphene, e.g. in reference [7]. The second option is aimed to reduce the sticking of graphene by using the solution with lower surface tension. IPA, for example, exhibits almost 4 times lower surface tension than water [79]. Further decrease in surface tension can be achieved by heating up the IPA. This procedure was used for graphene membranes by Du *et al.* [80].

Drying procedure, at the beginning of the experimental work, employed IPA heated up to ∼ 65 °C. Success rate of this process was between 10 % to 20 %. Two modifications were implemented to improve the drying procedure. New substrate,

[4]Specific temperature and pressure where there is no apparent difference between the liquid and gas state of a medium.

with 1 µm SiO_2 layer, allowed to etch deeper tranches (≈ 400 nm). This was aimed to reduce the possibility of graphene attaching to the bottom of the trench. Second, new heater with automatic temperature control was utilized for IPA heating. Precise control allowed to increase the temperature of the IPA to 78 °C without the risk of reaching the boiling point (≈ 82 °C). Success rate of improved manufacturing procedure was between 60 % to 80 % and an example of the suspended membrane is shown in the Fig. 4.11 b. Additional advantage of increased temperature of the IPA was removal of the PMMA layer. This eliminates the necessity of additional cleaning procedure to remove the resist layer after etching.

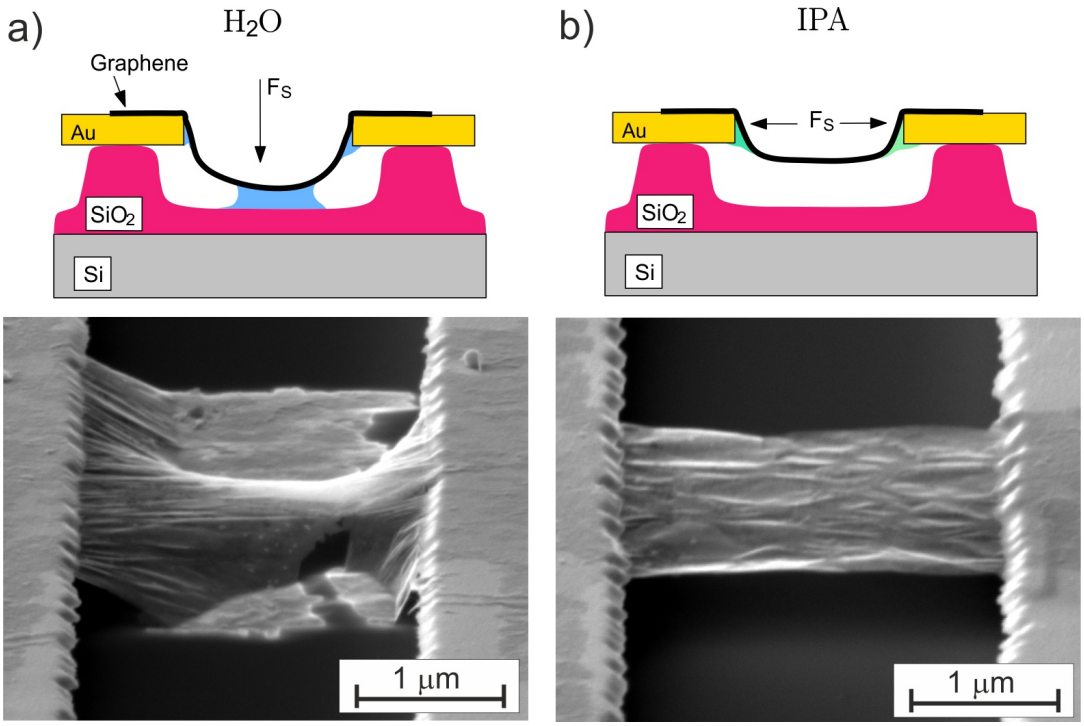

Fig. 4.11: a) Illustration of the drying process with water and SEM image of raptured graphene membrane attached to the substrate. Destruction of the device is presumed to be caused by the surface tension. b) Drying process with IPA and SEM image of successfully suspended graphene.

4.5.2 Graphene/SiO_2 interface

The described manufacturing process is possible due to additional features of graphene, that we have not discussed in the previous sections. Graphene exhibits strong adhesion even with the smoothest substrates [81]. This ability is attributed to the extreme flexibility of graphene, which allows it to conform to the topography and therefore increase van der Waals interaction forces with the substrate. Such

behaviour is beneficial in fixation of graphene on the gold electrodes. Additionally, the HF acid was observed to homogeneously etch SiO_2 underneath the grapheme. Normally, the BHF works as an isotropic etchant and therefore the underetching of graphene would be the same as for the gold electrodes. This would impose significant limits to the possible sizes of the membranes, due to the mechanical instability of the device. Underetching of the electrodes is shown in the Fig. 4.12, it is visible that electrodes are underetched by approximately the same amount as the depth of the trench ($\approx 300\,\mathrm{nm}$). On the other hand, the graphene membranes in the Fig. 4.11 have width in several micrometres. It was suggested that HF propagates along the graphene/SiO_2 interface [7], therefore the uniform SiO_2 etching underneath the graphene proceeds as if no graphene layer was present.

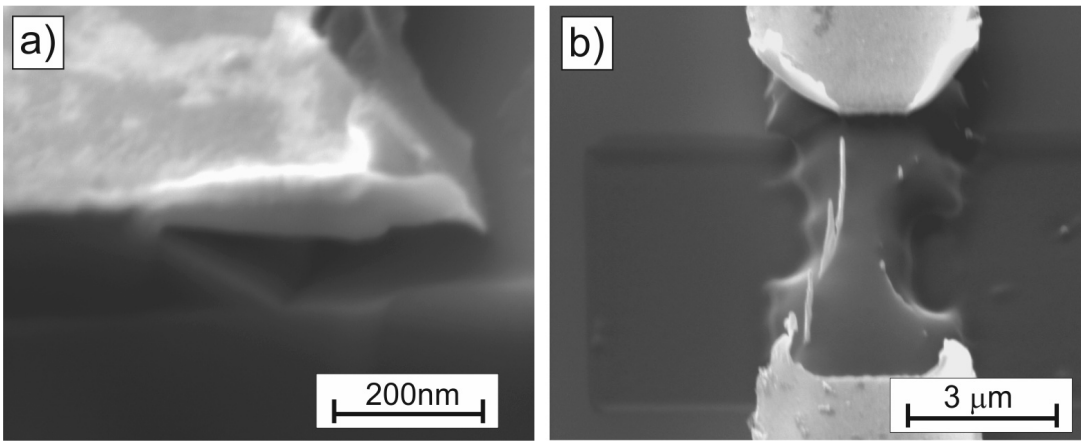

Fig. 4.12: SEM images of the underetched golden electrodes. a) A side view of the electrode cut by focused ion beam. b) Top view of the electrode with gold layer partially removed by FIB. Inhomogeneous underetching of electrode can be observed.

5 TRANSPORT MEASUREMENTS

5.1 Measurement configuration

Final device was attached to the sample holder (Fig. 5.1) by conductive silver epoxy paste. Golden electrodes, connected to the graphene membranes on SiO_2, were linked to the sample holder by 30 µm thick gold wires. Connection was fabricated by the TPT Wire Bonder HB 16, which utilizes an ultrasonic bonding.

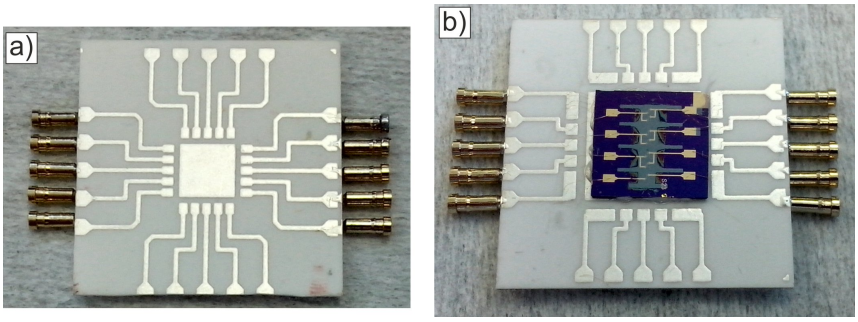

Fig. 5.1: a) Design of ceramic sample holder with conductive paths. b) A sample attached to the holder by silver epoxy paste. Golden electrodes were connected using 30 µm thick gold wires attached by ultrasonic bonding.

The scheme of the configuration for transport measurements is shown in Fig. 5.2. The resistance of the graphene layer was measured by Lock-In amplifier Stanford SR830. Lock-In generated sinusoidal signal with amplitude 1 V and operational frequency of 13.33 kHz was kept constant during the measurements. Additionally, the current was reduced by attaching serial 10 MΩ resistor to prevent damage of the membrane. Therefore, current amplitude was ~ 100 nA.

In order to induce the change in charge carrier concentration of graphene membrane, the gate voltage (V_G) was applied to the Si substrate. The gate voltage value was controlled by Keithely 6221AC current source. Voltage was applied as a potential drop on the 1 MΩ resistor, e.g. voltage 10 V was obtained by a current of 10 µA. To reduce the electrical noise all the connections to the devices were carried out with shielded coaxial cables. Both the Stanford Lock-In amplifier and Keithely current source were connected to the computer by the GPIB (General Purpose Interface Bus). Measurements were automatized and controlled by LabVIEW software.

Before the measurements were performed it had been necessary to check for the leakage current between the back gate and top electrodes. The leakage current can be caused by defects in the isolation layer, underetched electrodes or graphene overhang. To reduce the leakage, it became necessary to remove graphene surrounding the electrodes, as described in section 4.4.

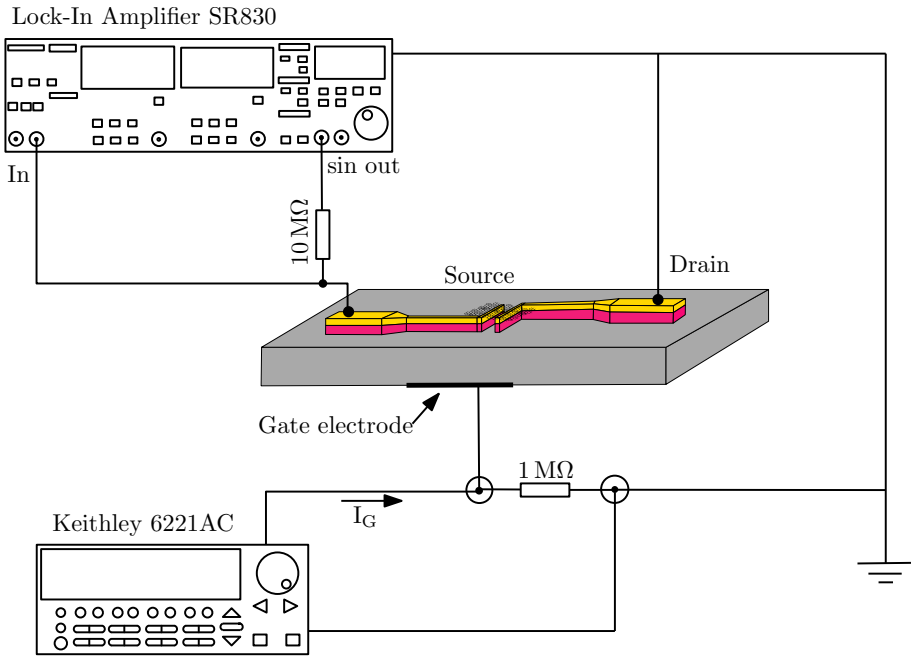

Fig. 5.2: Schematics of the transport measurements configuration for device in FET configuration. Gate voltage is applied by Keithely current source as a voltage drop on 1 MΩ resistor. Resistance of the graphene layer is measured by Stanford Lock-In amplifier. Alternating voltage with amplitude 1 V is applied at 133 kHz frequency.

5.2 Graphene membrane

The recorded resistivity of the graphene membrane (R) was converted to the conductance by equation

$$\sigma = \left(\frac{L}{W}\right)\frac{1}{R}, \tag{5.1}$$

where L and W are length and width of the membrane obtained from SEM image. Membrane length was usually 2.8 µm and width varied from 1 to 15 µm. Typical shape of conductance dependency on the gate voltage is shown in the Fig. 5.3 a. In comparison with an ideal graphene the Dirac point is not clearly distinguishable. Position of the Dirac point was approximately −3 V. All measured membranes had similar peaks, or rather plateaus, around the same value. This implies that the graphene layer is p-doped. Graphene placed on SiO_2 substrate also exhibited strong p-doping (e.g. ref. [82]). This was also observed by Procházka *et al.* [73] for CVD graphene manufactured at our institute by similar procedure.

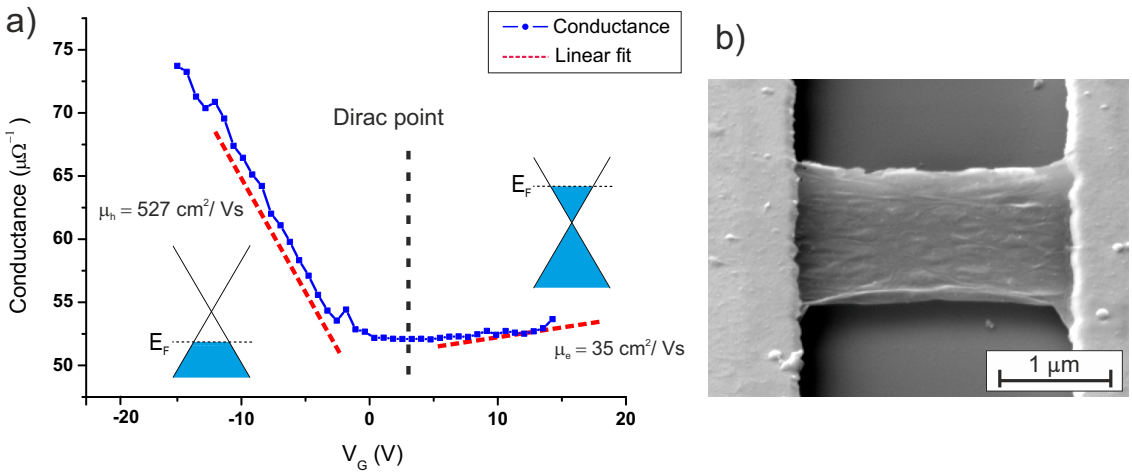

Fig. 5.3: a) Measured conductance dependence on the gate voltage (blue line), for graphene membrane in FET configuration. Electron and hole mobility is calculated from the slope of the linear fits (red lines). Inset illustrations show supposed position of the Fermi level in graphene. b) SEM image of a measured graphene membrane.

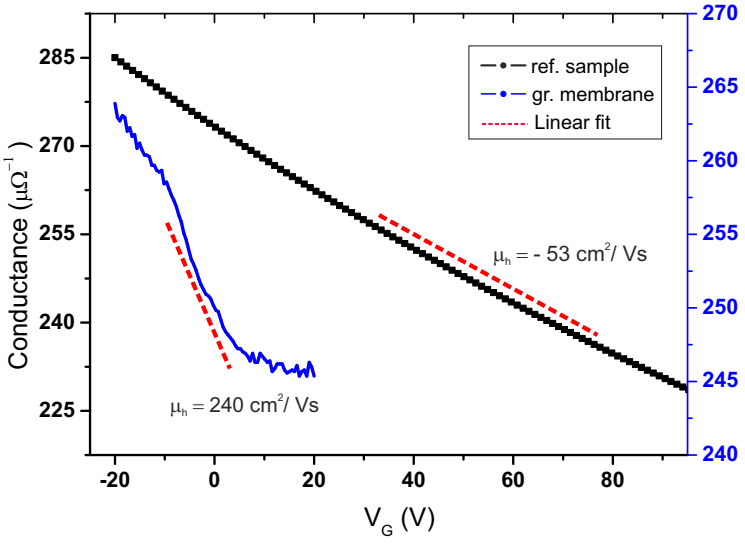

Fig. 5.4: Measured conductance dependence on the gate voltage of reference sample consisting from graphene placed on the SiO_2 substrate (black line). Measurement of graphene membrane (blue line) with similar conductance is shown for comparison. Linear fit of $\sigma(V_G)$ is marked in red and corresponding charge carrier mobilities are $240\,\mathrm{cm^2V^{-1}s^{-1}}$ for membrane and $53\,\mathrm{cm^2V^{-1}s^{-1}}$ for reference sample.

Additional information obtained from conductance measurements is the charge carrier mobility of graphene. It was described in the second chapter about graphene transport properties (sec. 2.1.1) that mobility can be extracted from the slope (α) of $\sigma(V_G)$ dependency

$$\mu_{FE} = \frac{\alpha\, d}{\varepsilon_0\, \varepsilon}, \tag{5.2}$$

where ε is relative permittivity of isolating material (SiO_2 or air), ε_0 is the permittivity of vacuum and d thickness of the insulating layer. The slope α is obtained from linear fit as shown in Fig. 5.3 a. Unbalanced conductance of graphene can be explained as high mobility of holes and low mobility of electrons. Calculated mobilities of holes was in range from 96 to 527 $cm^2V^{-1}s^{-1}$ and average value of $234 \pm 98\, cm^2V^{-1}s^{-1}$.

Reference samples of graphene on SiO_2 substrate were prepared with the same procedure except of the chemical etching. Dirac point cannot be distinguished up to 100V. Higher gate voltage was not attempted, due to the concerns about reaching breakdown current of insulating layer and damaging the equipment. Estimated hole mobility was $\sim 53\, cm^2V^{-1}s^{-1}$ as shown in Fig.5.4. Such a value could mean that quadruple improvement in mobility was achieved. On the other hand, the mobilities measured for similar graphene devices, fabricated by the same CVD procedure and measured by J. Piastek achieved mobility $165\, cm^2V^{-1}s^{-1}$ [83] and measurements performed by J. Hulva in 2014 yielded mobilities $35, 131$ and $605\, cm^2V^{-1}s^{-1}$ [84].

Thickness of dielectric layer

Important parameter for calculation of the charge carrier mobility (Eq. (5.2)) is thickness (d) of the dielectric material. In conventional graphene devices the dielectric geometry is strictly defined. On the other hand, in suspended graphene device (Fig. 5.5 a), the thickness of insulating layer depends on the membrane bending and amount of the etched material.

The values for calculation of charge carrier mobilities were determined from AFM topography (see Fig.5.5 c, d). Depth of the trench (D) includes the thickness of the gold layer (70 nm) and depth of the etched material. AFM measurements were also used to determine the membrane bending, but they resulted in the membrane rupture. Therefore, SEM measurements from the side (high angle) were performed. Sample was tilted to $\sim 89°$ as can be seen in the Fig.5.5 b. Membrane appeared to be almost at the same level as bottom of the electrodes. Therefore the bending of the membrane in calculations was estimated to 30 nm. For devices on samples with 280 nm thick SiO_2 layer, the complete removal of SiO_2 was usually observed. Therefore, these samples were regarded as single capacitors with a 250 nm thick insulating layer of air.

The devices with 1 µm thick SiO_2 layer, had insulating layer composed from 400 nm layer of air and 570 nm layer of SiO_2. Since the calculation of the mobility in graphene on SiO_2 is derived from single parallel plate capacitor model, multilayer devices have to be regarded as two capacitors connected in series. The equation (5.2) is then rewritten as

$$\mu_{\mathrm{FE}} = \alpha \left(\frac{\varepsilon_1 d_2 + \varepsilon_2 d_1}{\varepsilon_1 \varepsilon_2 \varepsilon_0} \right), \tag{5.3}$$

where ε_1 and ε_2 are relative permitivities of the insulating materials with thicknesses d_1 and d_2. Only a few samples were measured by AFM, therefore, a slight variation of thicknesses could occur depending on the etching precision. Additionally, the electrostatic force between the gate electrode and the membrane can cause further bending [85]. To investigate this behaviour it would be beneficial to perform in-situ SEM measurements.

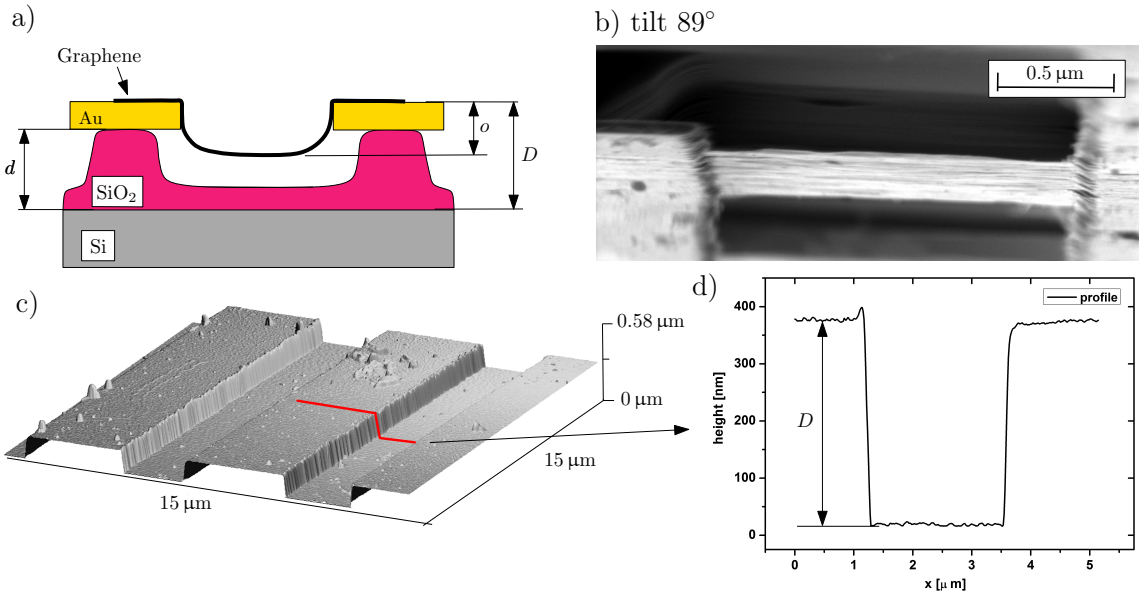

Fig. 5.5: a) Illustration of the cross section of graphene membrane device. b)An 89 ° angle SEM image of graphene membrane. c) 3D AFM topography of electrodes after chemical etching. d) Measured AFM profile of the etched trench with depth D.

5.3 Heating of membrane

In an attempt to further increase the charge carrier mobility of graphene, fabricated membranes were heated to 130 °C on a hot plate in ambient conditions. This procedure should induce desorption of gases from the graphene surface [24]. Lower

temperature heating was meant as an intermediate step before attempting the annealing at 300 °C to remove the PMMA residues.

Graphene membranes were heated for approximately 40 min which resulted in increased conductance, shown in the Fig.5.6 a. Such a change corresponds to only about 30 Ω decrease in resistance. Charge carrier mobility changed insignificantly from 179 to 183 $cm^2V^{-1}s^{-1}$. Further, the resistance of the membrane was slowly increasing back to its original value, which is attributed to the reabsorption of ambient gases.

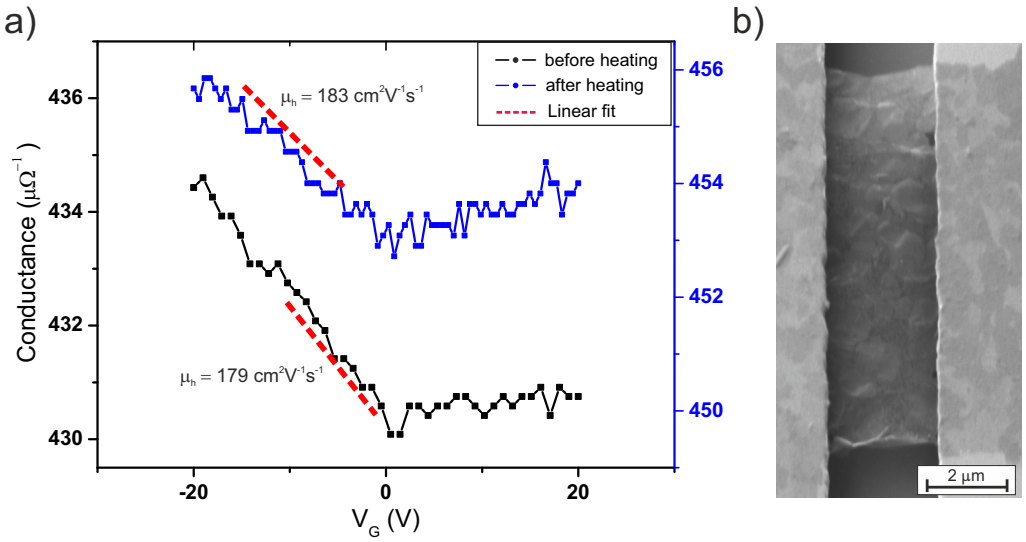

Fig. 5.6: a) Measured conductance dependence on the gate voltage for graphene membrane before (black line) and after 40 min at 130 °C (blue line). b) SEM image of measured graphene membrane.

Most of the membranes showed to be partially or completely ruptured after heating. This could be attributed to the shortening of the graphene during heating as was described in the third chapter (sec. 3.1.2). The change of the length was estimated from the graphene expansion coefficient to be only few nanometres for a micrometre membrane. Therefore, the reason of damaging the membranes during heating was not proved and needs to be investigated further. The rupturing of the membranes impeded all future experiments. This behaviour needs to be avoided in order to test the sensing properties of graphene membrane or attempt high temperature annealing of graphene to increase its charge carrier mobility.

Two of the devices exhibited interesting behaviour after the heating. In spite of extreme values of their resistivity (in MΩ), strong reaction to gate voltage was observed. One of these devices is shown in Fig. 5.7. The conductance exhibits area of minimal conductivity from 0 to -4 V of V_G corresponding to resistance over 4 MΩ, which is on the detection limit of our device. Repeated measurements showed further

increase of resistivity. Similar transport gap was observed by Molitor *et al.* [86] for graphene nano-ribbons with width $\leq$ 100 nm and contributed to the creation of band gap in graphene. Therefore, it is speculated that damaged membrane shown in Fig.5.7 d, was not completely ruptured and contained small conductive channel in order of nanometres. Since the graphene is lying on the insulating layer and actual dimensions of conductive channel could not be distinguished from SEM image, charge carrier mobilities for this device were not calculated.

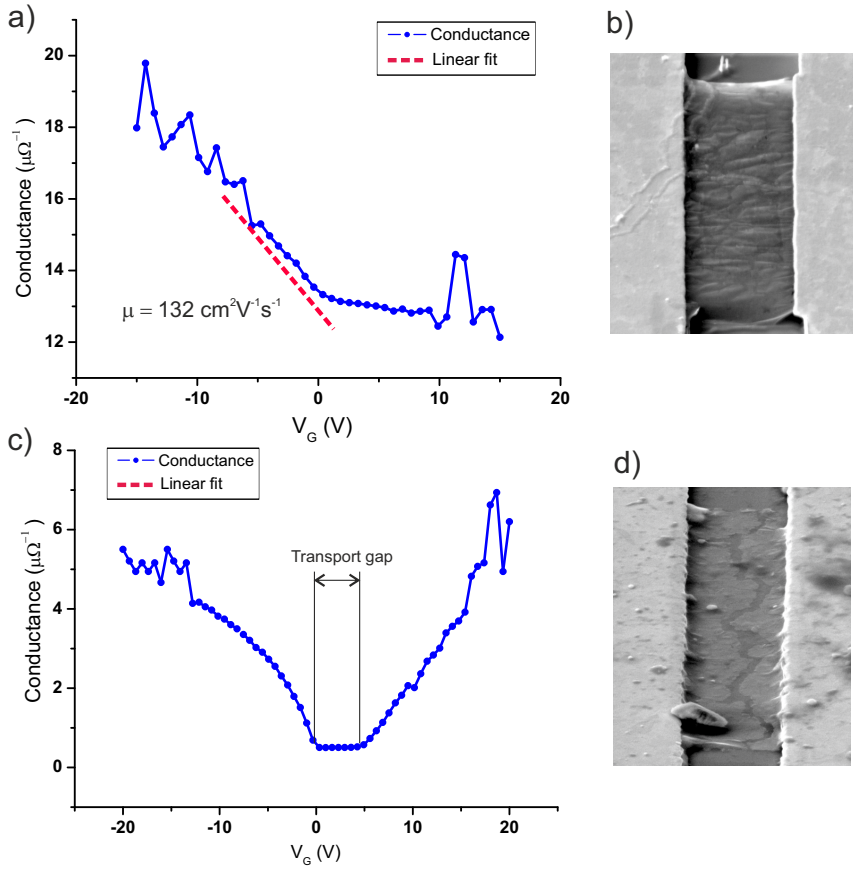

Fig. 5.7: a) Measured conductance dependence on the gate voltage for graphene membrane with mobility of 132 $\mathrm{cm^2V^{-1}s^{-1}}$ and b) corresponding SEM image. c) Change in the conductance after heating of the membrane at 130 °C. Conductance of the membrane decreased significantly. Additionally, wide plateau of minimal conductivity appeared, which is atributed to band gap of suspected narrow channel in membrane damaged during heating. d) SEM image of ruptured membrane.

6 CONCLUSIONS

This work was dedicated to the fabrication and characterisation of CVD graphene membranes. Theoretical part of the work was focused on transport properties of graphene, mostly the charge carrier mobility, which is often used as the measure of graphene quality. The intrinsic mobility of charge carriers in graphene, limited only by electron-phonon scattering, was predicted to reach values up to $\sim 200\,000\,\mathrm{cm^2V^{-1}s^{-1}}$ at room temperature. The mobility, measured in realistic graphene devices, is often significantly reduced by scattering effects described in the second chapter. A strong influence on the mobility was also attributed to the substrate, which supports the graphene. Therefore, graphene membranes are presented as a suitable option to improve the transport properties of graphene.

The fabrication process of graphene membranes was implemented to fit the current possibilities at the Institute of Physical Engineering. The chapter 4 provides a description of the fabrication steps for graphene devices in FET configuration. The two top electrodes were fabricated by electron beam lithography. Afterwards, graphene grown by chemical vapor deposition was transferred on the sample and patterned by second lithography procedure followed by etching in oxygen plasma. Suspension of graphene was achieved by chemical etching of the SiO_2 substrate in buffered hydrofluoric acid (NH_4F:HF). Drying of the samples after etching has proven to be the critical point of the fabrication process. Isopropyl alcohol heated up to 78 °C combined with etching of 400 nm of SiO_2 rather than original 280 nm resulted in successful suspension for most of the membranes. This process was used to fabricate arrays of graphene membranes on each sample and a single membrane was isolated from the rest by focused ion beam.

Each of the single graphene membranes was characterised by transport properties measurements described in chapter five. Devices were measured in field effect transistor configuration. The change in the charge carrier concentration of graphene was achieved by applying gate voltage with assumption that graphene and the substrate are acting as a parallel plate capacitor. The charge carrier mobility was estimated from the conductance dependence on gate voltage. The calculated mobilities of holes had average value of $234 \pm 98\,\mathrm{cm^2V^{-1}s^{-1}}$ and the highest recorded mobility was $527\,\mathrm{cm^2V^{-1}s^{-1}}$. An increase in the hole mobility compared to the reference sample of graphene on SiO_2 was observed. On the other hand, the measured value is not significantly higher compared to the other measurements performed at the institute. This is attributed to the influence of PMMA residues from the manufacturing process. Experiments in literature usually employ additional cleaning in form of high temperature annealing (300°C) and can achieve mobility values one order of magnitude higher.

Experiments with lower temperature annealing (130°C) caused a partial or complete rupture of most of the membranes. In order to further improve graphene membranes transport properties, this behaviour needs to be understood and eliminated. However, the presented fabrication process for suspended graphene was very reliable and will provide a solid basis for future experiments. A potential solution of the membranes ruptures may be the utilization of large area single crystal CVD graphene, which provides better mechanical properties in comparison with the polycrystalline layers. Graphene membranes could help to distinguish the effects of substrate from other scattering sources present in CVD graphene. Moreover, the graphene membranes could be utilized as mechanical resonators (described in chapter 3) and further improvement of their electronic properties could result in a wide range of new applications.

BIBLIOGRAPHY

[1] Novoselov, K. S., Geim, a. K., Morozov, S. V., Jiang, D., Zhang, Y., Dubonos, S. V., Grigorieva, I. V., and Firsov, A. Electric field effect in atomically thin carbon films. *Science (New York, N.Y.) 306*, 5696 (2004), 666–669. doi:10.1126/science.1102896.

[2] Novoselov, K. S., Geim, a. K., Morozov, S. V., Jiang, D., Katsnelson, M. I., Grigorieva, I. V., Dubonos, S. V., and Firsov, A. Two-dimensional gas of massless Dirac fermions in graphene. *Nature 438*, 7065 (2005), 197–200. doi:10.1038/nature04233.

[3] Lee, C., Wei, X., Kysar, J. W., and Hone, J. Measurement of the elastic properties and intrinsic strength of monolayer graphene. *Science (New York, N.Y.) 321*, 5887 (2008), 385–388. doi:10.1126/science.1157996.

[4] Nobelprize.org. The nobel prize in physics 2010. online, accessed: 22th May 2015. url:http://www.nobelprize.org/nobel_prizes/physics/laureates/2010/.

[5] Lin, Y., Dimitrakopoulos, C., Jenkins, K. a., Farmer, D. B., Chiu, H., Grill, a., and Avouris, P. 100-GHz transistors from wfer-scale epitaxial graphene. *Nano 327*, 5966 (2010), 100. doi:10.1126/science.1184289.

[6] Chen, J.-H., Jang, C., Xiao, S., Ishigami, M., and Fuhrer, M. S. Intrinsic and extrinsic performance limits of graphene devices on SiO2. *Nature nanotechnology 3*, 4 (2008), 206–209. doi:10.1038/nnano.2008.58.

[7] Bolotin, K. I., Sikes, K. J., Jiang, Z., Klima, M., Fudenberg, G., Hone, J., Kim, P., and Stormer, H. L. Ultrahigh electron mobility in suspended graphene. *Solid State Communications 146* (2008), 351–355. doi:10.1016/j.ssc.2008.02.024.

[8] Bae, S., Kim, H., Lee, Y., Xu, X., Park, J.-S., Zheng, Y., Balakrishnan, J., Lei, T., Kim, H. R., Song, Y. I., Kim, Y.-J., Kim, K. S., Ozyilmaz, B., Ahn, J.-H., Hong, B. H., and Iijima, S. Roll-to-roll production of 30-inch graphene films for transparent electrodes. *Nature nanotechnology 5*, 8 (2010), 574–578. doi:10.1038/nnano.2010.132.

[9] Pierson, H. *Handbook of Carbon, Graphite, Diamond and Fullerenes - Properties, Processing and Applications*. William Andrew Publishing/Noyes, 1993. ISBN 978-0-8155-1339-1.

[10] ChemWiki. The dynamic chemistry e-textbook. online, accessed: 22th May 2015. url:http://chemwiki.ucdavis.edu.

[11] Kroto, H. W., Heath, J. R., O'Brien, S. C., Curl, R. F., and Smalley, R. E. C 60: buckminsterfullerene. *Nature 318* (1985), 162. doi:10.1038/318162a0.

[12] Iijima, S. Helical microtubules of graphitic carbon. *Nature 354*, 6348 (1991), 56–58. doi:10.1038/354056a0.

[13] Elias, D. C., Nair, R. R., Mohiuddin, T. M. G., Morozov, S. V., Blake, P., Halsall, M. P., Ferrari, A. C., Boukhvalov, D. W., Katsnelson, M. I., Geim, A. K., and Novoselov, K. S. Control of graphene's properties by reversible hydrogenation: evidence for graphane. *Science (New York, N.Y.) 323*, 5914 (2009), 610–613. doi:10.1126/science.1167130.

[14] Zhang, S., Zhou, J., Wang, Q., Chen, X., Kawazoe, Y., and Jena, P. Penta-graphene: A new carbon allotrope. *Proceedings of the National Academy of Sciences* (2015), 201416591. doi:10.1073/pnas.1416591112.

[15] Badding, J. V., and Crespi, V. H. Synthesizing carbon nanothreads from benzene. *SPIE Newsroom 3* (2015), 10–12. doi:10.1117/2.1201501.005713.

[16] Castro Neto, H., Peres, N. M. R., Novoselov, K. S., and Geim, K. The electronic properties of graphene. *Reviews of Modern Physics 81*, 1 (2009), 109–162. doi:10.1103/RevModPhys.81.109.

[17] Wallace, P. R. The band theory of graphite. *Physical Review 71*, 9 (1947), 622–634. doi:10.1103/PhysRev.71.622.

[18] Partoens, B., and Peeters, F. M. From graphene to graphite: Electronic structure around the K point. *Physical Review B - Condensed Matter and Materials Physics 74*, 7 (2006), 1–11. doi:10.1103/PhysRevB.74.075404.

[19] Savage, N. Graphene makes transistors tunable. online, accessed: 20th May 2015. url:http://spectrum.ieee.org/semiconductors/materials/graphene-makes-transistors-tunable.

[20] Beenakker, C. W. J. Colloquium: Andreev reflection and Klein tunneling in graphene. *Reviews of Modern Physics 80*, 4 (2008), 1337–1354. doi:10.1103/RevModPhys.80.1337.

[21] Gusynin, V. P., and Sharapov, S. G. Unconventional integer quantum hall effect in graphene. *Physical Review Letters 95*, 14 (2005), 2–5. doi:10.1103/PhysRevLett.95.146801.

[22] Blake, P., Hill, E. W., Castro Neto, A. H., Novoselov, K. S., Jiang, D., Yang, R., Booth, T. J., and Geim, A. K. Making graphene visible. *Applied Physics Letters*, 6 (2007), 270–274. doi:10.1063/1.2768624.

[23] Geim, a. K., Novoselov, K. S., Geim A. K., and Novoselov K. S. The rise of graphene. *Nat. Mater.* (2007), 183–191. doi:http://dx.doi.org/10.1038/nmat1849.

[24] Schedin, F., Geim, a. K., Morozov, S. V., Hill, E. W., Blake, P., Katsnelson, M. I., and Novoselov, K. S. Detection of individual gas molecules adsorbed on graphene. *Nature materials 6*, 9 (2007), 652–655. doi:10.1038/nmat1967.

[25] Janssen, T. J. B. M., Tzalenchuk, a., Lara-Avila, S., Kubatkin, S., and Fal'ko, V. I. Quantum resistance metrology using graphene. *Reports on progress in physics. Physical Society (Great Britain) 76*, 10 (2013), 104501. doi:10.1088/0034-4885/76/10/104501.

[26] Güttinger, J., Molitor, F., Stampfer, C., Schnez, S., Jacobsen, a., Dröscher, S., Ihn, T., and Ensslin, K. Transport through graphene quantum dots. *Reports on progress in physics. Physical Society (Great Britain) 75*, 12 (2012), 126502. doi:10.1088/0034-4885/75/12/126502.

[27] Ando, T. Screening effect and impurity scattering in monolayer graphene. *Journal of the Physical Society of Japan 75*, 7 (2006), 1–7. doi:10.1143/JPSJ.75.074716.

[28] Chen, J.-H., Jang, C., Adam, S., Fuhrer, M. S., Williams, E. D., and Ishigami, M. Charged-impurity scattering in graphene. *Nature Physics 4*, 5 (2008), 377–381. doi:10.1038/nphys935.

[29] Adam, S., Hwang, E. H., Galitski, V. M., and Das Sarma, S. A self-consistent theory for graphene transport. *Proceedings of the National Academy of Sciences of the United States of America 104*, 47 (2007), 18392–18397. doi:10.1073/pnas.0704772104.

[30] Banhart, F., Kotakoski, J., and Krasheninnikov, A. V. Structural defects in graphene. *ACS Nano 5*, 1 (2011), 26–41. doi:10.1021/nn102598m.

[31] Qi, X., Guo, X., and Zheng, C. Density functional study the interaction of oxygen molecule with defect sites of graphene. *Applied Surface Science 259* (2012), 195–200. doi:10.1016/j.apsusc.2012.07.018.

[32] Jauregui, L. a., Cao, H., Wu, W., Yu, Q., and Chen, Y. P. Electronic properties of grains and grain boundaries in graphene grown by chemical vapor deposition. *Solid State Communications 151*, 16 (2011), 1100–1104. doi:10.1016/j.ssc.2011.05.023.

[33] Huang, P. Y., Ruiz-Vargas, C. S., van der Zande, A. M., Whitney, W. S., Levendorf, M. P., Kevek, J. W., Garg, S., Alden, J. S., Hustedt, C. J., Zhu, Y., Park, J., McEuen, P. L., and Muller, D. Grains and grain boundaries in single-layer graphene atomic patchwork quilts. *Nature 469*, 7330 (2011), 389–392. doi:10.1038/nature09718.

[34] Morozov, S. V., Novoselov, K. S., Katsnelson, M. I., Schedin, F., Elias, D. C., Jaszczak, J. a., and Geim, a. K. Giant intrinsic carrier mobilities in graphene and its bilayer. *Physical Review Letters 100*, 1 (2008), 11–14. doi:10.1103/PhysRevLett.100.016602.

[35] Hwang, E. H., and Das Sarma, S. Acoustic phonon scattering limited carrier mobility in two-dimensional extrinsic graphene. *Physical Review B - Condensed Matter and Materials Physics 77*, 11 (2008), 1–6. doi:10.1103/PhysRevB.77.115449.

[36] Das Sarma, S., Adam, S., Hwang, E. H., and Rossi, E. Electronic transport in two-dimensional graphene. *Reviews of Modern Physics 83*, 2 (2011), 407–470. doi:10.1103/RevModPhys.83.407.

[37] Bolotin, K. I. Electronic transport in graphene: towards high mobility. In *Graphene*, V. Skakalova and A. B. Kaiser, Eds. Woodhead Publishing, 2014, ch. 9, pp. 199 – 227. ISBN 978-0-85709-508-4.

[38] Lin, Y. C., Jin, C., Lee, J. C., Jen, S. F., Suenaga, K., and Chiu, P. W. Clean transfer of graphene for isolation and suspension. *ACS Nano 5*, 3 (2011), 2362–2368. doi:10.1021/nn200105j.

[39] Lin, Y. C., Lu, C. C., Yeh, C. H., Jin, C., Suenaga, K., and Chiu, P. W. Graphene annealing: How clean can it be? *Nano Letters 12*, 1 (2012), 414–419. doi:10.1021/nl203733r.

[40] Dean, C. R., Young, a. F., Meric, I., Lee, C., Wang, L., Sorgenfrei, S., Watanabe, K., Taniguchi, T., Kim, P., Shepard, K. L., and Hone, J. Boron nitride substrates for high-quality graphene electronics. *Nature nanotechnology 5*, 10 (2010), 722–726. doi:10.1038/nnano.2010.172.

[41] Mayorov, A. S., Gorbachev, R. V., Morozov, S. V., Britnell, L., Jalil, R., Ponomarenko, L. A., Blake, P., Novoselov, K. S., Watanabe, K., Taniguchi, T., and Geim, A. K. Micrometer-scale ballistic transport in encapsulated graphene at room temperature. *Nano Letters 11*, 6 (2011), 2396–2399. doi:10.1021/nl200758b.

[42] Lee, J.-H., Loya, P. E., Lou, J., and Thomas, E. L. Dynamic mechanical behavior of multilayer graphene via supersonic projectile penetration. *Science (New York, N.Y.) 1092* (2014). doi:10.1126/science.1258544.

[43] Romao, C., Miller, K., Whitman, C., White, M., and Marinkovic, B. *Comprehensive Inorganic Chemistry II*. Elsevier, 2013. ISBN 9780080965291.

[44] Jiang, J.-W., Wang, J.-S., and Li, B. Thermal expansion in single-walled carbon nanotubes and graphene: Nonequilibrium Green's function approach. *Physical Review B 80*, 20 (Nov. 2009), 205429. doi:10.1103/PhysRevB.80.205429.

[45] Yoon, D., Son, Y.-W., and Cheong, H. Negative thermal expansion coefficient of graphene measured by Raman spectroscopy. *Nano letters 11*, 8 (2011), 3227–3231. doi:10.1021/nl201488g.

[46] Bao, W., Miao, F., Chen, Z., Zhang, H., Jang, W., Dames, C., and Lau, C. N. Controlled ripple texturing of suspended graphene and ultrathin graphite membranes. *Nature nanotechnology 4*, 9 (2009), 562–566. doi:10.1038/nnano.2009.191.

[47] Meyer, J. C., Girit, C. O., Crommie, M. F., and Zettl, a. Imaging and dynamics of light atoms and molecules on graphene. *Nature 454*, 7202 (2008), 319–322. doi:10.1038/nature07094.

[48] Tedpella.com. Graphene tem support films. online, 2015, accessed: 22th May 2015. url:http://www.tedpella.com/support_films_html/graphene-tem-support-film.htm.aspx#graphene_films.

[49] High-Resolution EM of colloidal nanocrystal growth using graphene liquid Cells. *Science 336*, 6077 (2012), 61–64. doi:10.1126/science.1217654.

[50] Bunch, J. S., Verbridge, S. S., Alden, J. S., Van Der Zande, A. M., Parpia, J. M., Craighead, H. G., and McEuen, P. L. Impermeable atomic membranes from graphene sheets. *Nano Letters 8* (2008), 2458–2462. doi:10.1021/nl801457b.

[51] Hashimoto, A., Suenaga, K., Gloter, A., Urita, K., and Iijima, S. Direct evidence for atomic defects in graphene layers. *Nature 430*, 7002 (2004), 870–873. doi:10.1038/nature02817.

[52] O'Hern, S. C., Boutilier, M. S. H., Idrobo, J. C., Song, Y., Kong, J., Laoui, T., Atieh, M., and Karnik, R. Selective ionic transport through tunable subnanometer pores in single-layer graphene membranes. *Nano Letters 14* (2014), 1234–1241. doi:10.1021/nl404118f.

[53] Cohen-Tanugi, D., and Grossman, J. C. Water desalination across nanoporous graphene. *Nano Letters 12*, 7 (2012), 3602–3608. doi:10.1021/nl3012853.

[54] Surwade, S. P., Smirnov, S. N., Vlassiouk, I. V., Unocic, R. R., Veith, G. M., Dai, S., and Mahurin, S. M. Water desalination using nanoporous single-layer graphene. *Nature Nanotechnology 10*, 5 (2015), 459–464. doi:10.1038/nnano.2015.37.

[55] Mahmoud, K. A., Mansoor, B., Mansour, A., and Khraisheh, M. Functional graphene nanosheets: The next generation membranes for water desalination. *Desalination 356* (2014), 208–225. doi:10.1016/j.desal.2014.10.022.

[56] Wang, Y., Zhou, Z., Yang, Z., Chen, X., Xu, D., and Zhang, Y. Gas sensors based on deposited single-walled carbon nanotube networks for DMMP detection. *Nanotechnology 20*, 34 (2009), 345502. doi:10.1088/0957-4484/20/34/345502.

[57] Edel, J., and Albrecht, T. *Engineered Nanopores for Bioanalytical Applications*, 1 ed. Elsevier Inc., 2013. ISBN 9781437734737.

[58] Schneider, G. F., Kowalczyk, S. W., Calado, V. E., Pandraud, G., Zandbergen, H. W., Vandersypen, L. M. K., and Dekker, C. DNA Translocation through Grapheme Nanopores. *Nano Letters 10*, 8 (2010), 3163–3167. doi:10.1021/nl102069z.

[59] Liu, F., Ming, P., and Li, J. Ab initio calculation of ideal strength and phonon instability of graphene under tension. *Physical Review B - Condensed Matter and Materials Physics 76*, 6 (2007), 1–7. doi:10.1103/PhysRevB.76.064120.

[60] Bae, S. H., Lee, Y., Sharma, B. K., Lee, H. J., Kim, J. H., and Ahn, J. H. Graphene-based transparent strain sensor. *Carbon 51*, 1 (2013), 236–242. doi:10.1016/j.carbon.2012.08.048.

[61] Smith, A. D., Vaziri, S., Niklaus, F., Fischer, A. C., Sterner, M., Delin, A., Östling, M., and Lemme, M. C. Pressure sensors based on suspended graphene membranes. *Solid-State Electronics 88* (2013), 89–94. doi:10.1016/j.sse.2013.04.019.

[62] Smith, a. D., Niklaus, F., Paussa, a., Vaziri, S., Fischer, a. C., Sterner, M., Forsberg, F., Delin, a., Esseni, D., Palestri, P., Östling, M., and Lemme, M. C. Electromechanical piezoresistive sensing in suspended graphene membranes. *Nano Letters 13* (2013), 3237–3242. doi:10.1021/nl401352k.

[63] Tooley, M., and Tooley, M. *Electronic Circuits: Fundamentals and Applications*. Elsevier, 2006. ISBN 9780750669238.

[64] Eichler, a., Moser, J., Chaste, J., Zdrojek, M., Wilson-Rae, I., and Bachtold, a. Nonlinear damping in mechanical resonators made from carbon nanotubes and graphene. *Nature nanotechnology 6*, 6 (2011), 339–342. doi:10.1038/nnano.2011.71.

[65] Bunch, J. S., van der Zande, A. M., Verbridge, S. S., Frank, I. W., Tanenbaum, D. M., Parpia, J. M., Craighead, H. G., and McEuen, P. L. Electromechanical resonators from graphene sheets. *Science (New York, N.Y.) 315*, 5811 (2007), 490–493. doi:10.1126/science.1136836.

[66] Chen, C., Rosenblatt, S., Bolotin, K. I., Kalb, W., Kim, P., Kymissis, I., Stormer, H. L., Heinz, T. F., and Hone, J. Performance of monolayer graphene nanomechanical resonators with electrical readout. *Nature nanotechnology 4*, 12 (2009), 861–867. doi:10.1038/nnano.2009.267.

[67] Chen, C., Lee, S., Deshpande, V. V., Lee, G.-H., Lekas, M., Shepard, K., and Hone, J. Graphene mechanical oscillators with tunable frequency. *Nature nanotechnology 8*, 12 (2013), 923–7. doi:10.1038/nnano.2013.232.

[68] Konečný, M. Application of KPM on graphene/Si substrate modified by FIB method. Master's thesis, Brno University of Technology, 53s, 2013.

[69] Li, X., Cai, W., An, J., Kim, S., Nah, J., Yang, D., Piner, R., Velamakanni, A., Jung, I., Tutuc, E., Banerjee, S. K., Colombo, L., and Ruoff, R. S. doi:10.1126/science.1171245.

[70] Kumar, A., and Lee, C. H. Synthesis and Biomedical Applications of Graphene : Present and Future Trends. *Advances in Graphene Science* (2013), 55–75. doi:10.5772/55728.

[71] Yan, Z., Lin, J., Peng, Z., Sun, Z., Zhu, Y., Li, L., Xiang, C., Samuel, E. L., Kittrell, C., and Tour, J. M. Toward the synthesis of wafer-scale single-crystal graphene on copper foils. *ACS Nano 6*, 10 (2012), 9110–9117. doi:10.1021/nn303352k.

[72] Procházka, P., Mach, J., Bischoff, D., Lišková, Z., Dvořák, P., Vaňatka, M., Simonet, P., Varlet, A., Hemzal, D., Petrenec, M., Kalina, L., Bartošík, M., Ensslin, K., Varga, P., Čechal, J., and Šikola, T. Ultrasmooth metallic foils for growth of high quality graphene by chemical vapor deposition. *Nanotechnology 25*, 18 (2014), 185601. doi:10.1088/0957-4484/25/18/185601.

[73] Procházka, P. The preparation of graphene by the method CVD. Master's thesis, Brno University of Technology, 65s, 2012.

[74] Rai-Choudhury, P. *Handbook of Microlithography, Micromachining, and Microfabrication*, vol. 1: Microlithography. SPIE Press, 1997. ISBN 9780819423788.

[75] Babocky, J. Optical response of asymmertic plasmonic structures. Master thesis, Brno University of Technology, 52s, 2014.

[76] MicroChem. NANO PMMA and Copolymer. online, 2001, accessed: 22th May 2015.

[77] Williams, K. R., Gupta, K., and Wasilik, M. Etch rates for micromachining processing. *Journal of Microelectromechanical Systems 12*, 6 (2003), 761–778. doi:10.1109/JMEMS.2003.820936.

[78] Gap, B. H.-m.-s., Kim, S.-s., Kim, K.-s., Lee, H.-j., Choi, B.-i., Song, C.-k., Ahn, J.-h., and Al, L. Monatomic Chemical-Vapor- Deposited Graphene Membranes. *ACS nano 8*, Xx (2014), 2336–2344.

[79] Vasquez, G., Alvarez, E., and Navaza, J. M. Tension of Alcohol + Water from 20 to 50 °C. *Journal of Chemical and Engineering Data 40*, 3 (1995), 611–614. doi:10.1021/je00019a016.

[80] Du, X., Skachko, I., Barker, A., and Andrei, E. Y. Approaching ballistic transport in suspended graphene. *Nature nanotechnology 3* (2008), 491–495. doi:10.1038/nnano.2008.199.

[81] Koenig, S. P., Boddeti, N. G., Dunn, M. L., and Bunch, J. S. Ultrastrong adhesion of graphene membranes. *Nature nanotechnology 6*, 9 (2011), 543–546. doi:10.1038/nnano.2011.123.

[82] Pirkle, a., Chan, J., Venugopal, a., Hinojos, D., Magnuson, C. W., McDonnell, S., Colombo, L., Vogel, E. M., Ruoff, R. S., and Wallace, R. M. The effect of chemical residues on the physical and electrical properties of chemical vapor deposited graphene transferred to SiO2. *Applied Physics Letters 99*, 12 (2011), 2011–2014. doi:10.1063/1.3643444.

[83] Piastek, J. Preparation and Characterisation of Electrical Properties of Graphene Cvd Single Crystals, 54s, 2014.

[84] Hulva, J. Preparation and Characterisation of Electrical Properties of Graphene Cvd Single Crystals, 53s, 2014.

[85] Bao, W., Myhro, K., Zhao, Z., Chen, Z., Jang, W., Jing, L., Miao, F., Zhang, H., Dames, C., and Lau, C. N. In situ observation of electrostatic and thermal manipulation of suspended graphene membranes. *Nano Letters 12*, 11 (2012), 5470–5474. doi:10.1021/nl301836q.

[86] Molitor, F., Jacobsen, a., Stampfer, C., Güttinger, J., Ihn, T., and Ensslin, K. Transport gap in side-gated graphene constrictions. *Physical Review B - Condensed Matter and Materials Physics 79*, 7 (2009). doi:10.1103/PhysRevB.79.075426.

LIST OF ABBREVIATIONS

abbreviation	explanation
AFM	atomic force microscope
BHF	buffered hydrofluoric acid
CVD	chemical vapor deposition
DNA	deoxyribonucleic acid
EBL	electron beam lithography
FET	field effect transistor
GPIB	general purpose interface bus
hBN	hexagonal boron nitride
HF	hydrofluoric acid
IBS	ion beam sputtering
IPA	isopropyl alcohol
IQHE	integer quantum Hall effect
LIPIT	laser-induced projectile impact test
MIBK	methyl isobutyl ketone
MLG	multi layer graphene
NEMS	nanoelectromechanical systems
NTE	negative thermal expansion
PMMA	poly(methyl methacrylate)
RIP	remote interfacial phonon
RNA	ribonucleic acid
SEM	scanning electron microscope
TEC	thermal expansion coefficient
TEM	transmission electron microscope
UHV	ultra high vacuum